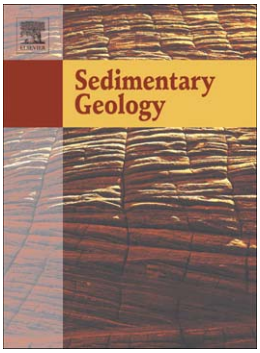

Sedimentology and geomorphology of a large tsunamigenic landslide, Taan Fiord, Alaska

A. Dufresne, M. Geertsema, D.H. Shugar, M. Koppes, B. Higman, P.J. Haeussler, C. Stark, J.G. Venditti, D. Bonno, C. Larsen, S.P.S. Gulick, N. McCall, M. Walton, M.G. Loso, M.J. Willis

PII: S0037-0738(17)30223-3
DOI: doi:10.1016/j.sedgeo.2017.10.004
Reference: SEDGEO 5247

To appear in: *Sedimentary Geology*

Received date: 28 May 2017
Revised date: 5 October 2017
Accepted date: 7 October 2017

Please cite this article as: Dufresne, A., Geertsema, M., Shugar, D.H., Koppes, M., Higman, B., Haeussler, P.J., Stark, C., Venditti, J.G., Bonno, D., Larsen, C., Gulick, S.P.S., McCall, N., Walton, M., Loso, M.G., Willis, M.J., Sedimentology and geomorphology of a large tsunamigenic landslide, Taan Fiord, Alaska, *Sedimentary Geology* (2017), doi:10.1016/j.sedgeo.2017.10.004

Sedimentology and geomorphology of a large tsunamigenic landslide, Taan Fiord, Alaska

A. Dufresne[1*], M. Geertsema[2], D.H. Shugar[3], M. Koppes[4], B. Higman[5], P.J. Haeussler[6], C. Stark[7], J.G. Venditti[8], D. Bonno[3], C. Larsen[9], S.P.S. Gulick[10], N. McCall[10], M. Walton[11], M.G. Loso[12], M.J. Willis[13]

[1]RWTH-Aachen University, Engineering Geology and Hydrogeology, Lochnerstr. 4-20, 52064 Aachen, Germany; [2]British Columbia Ministry of Forests, Lands and Natural Resource Operations, 499 George Street, Prince George, Canada; [3]Interdisciplinary Arts and Science, University of Washington Tacoma, 1900 Commerce St, Tacoma, WA, 98402, USA; [4]Department of Geography, University of British Columbia, 1984 West Mall, Vancouver, Canada; [5]Ground Truth Trekking, Seldova, Alaska, USA; [6]U.S. Geological Survey, 4210 University Drive, Anchorage, AK, USA; [7]Lamont-Doherty Earth Observatory, Columbia University, 305A Oceanography, 61 Route 9W, Palisades, NY, USA; [8]Department of Geography, Simon Fraser University, Burnaby, Canada; [9]Geophysical Institute, The University of Alaska Fairbanks, 903 Koyukuk Drive, Fairbanks, AK, USA; [10]Institute for Geophysics, University of Texas, 10100 Burnet Road, Austin, TX, USA; [11]USGS Pacific Coastal and Marine Science Center, 2885 Mission Street, Santa Cruz, CA, USA; [12]Wrangell-St. Elias National Park and Preserve and Central Alaska Inventory and Monitoring Network, Copper Center, AK, USA; [13]Cooperative Institute for Research in Environmental Sciences, University of Colorado Boulder, 216 UCB, Boulder, CO, USA

Abstract

On 17 October 2015, a landslide of roughly 60 x 10^6 m^3 occurred at the terminus of Tyndall Glacier in Taan Fiord, southeastern Alaska. It caused a tsunami that inundated an area over 20 km^2, whereas the landslide debris itself deposited within a much smaller area of approximately 2 km^2. It is a unique event in that the landslide debris was deposited into three very different environments: on the glacier surface, on land, and in the marine waters of the fjord. Part of the debris traversed the width of the fjord and re-emerged onto land, depositing coherent hummocks with preserved source stratigraphy on an alluvial fan and adjacent moraines on the far side of the fjord. Imagery from before the landslide shows that the catastrophic slope failure was preceded by deformation and sliding for at least the two decades since the glacier retreated to its current terminus location, exposing steep and extensively faulted slopes. A small volume of the total slide mass remains within the source area and is topped by striated blocks (> 10 m across) and standing trees that were transported down the slope in intact positions during the landslide. Field work was carried out in the summer of 2016, and by the time this paper was written, almost all of the supraglacial debris was advected into the fjord and half the subaerial hummocks were buried by glacial advance; this rapid change illustrates how highly active sedimentary processes in high-altitude glacial settings can skew any landslide-frequency analyses, and emphasizes the need for timely field investigations of these natural hazards.

Keywords: landslide, sedimentology, tsunami, Alaska, periglacial

1. Introduction

With retreating glaciers and permafrost degradation in high mountains, an increase in landslide activity can be expected (Gruber and Haeberli, 2007; McColl et al., 2012; Geertsema and Chiarle, 2013; Geertsema et al., 2013; Deline et al., 2015a, b; Kos et al., 2016; Coe et al., 2017: Grämiger et al., 2017). Glacier Bay National Park in southeastern Alaska—a landscape with many retreating glaciers—has seen at least eight large, long-runout landslides since 2012. The longer-term database of slope failure events is most likely incomplete due to rapid denudation of their deposits in these highly dynamic mountain and glacial environments (see also Shugar and Clague, 2011; Uhlmann et al., 2012;

Dunning et al., 2013; Coe et al., 2017). Seismologic detection and characterization of such events has significantly improved (Ekström and Stark, 2013) and led to the fast discovery of this remote landslide (Haeussler et al., 2017; Higman et al., submitted).

Landslides associated with catastrophic rockslope failures create deposits of highly fragmented debris with a number of characteristic sedimentologic and morphologic features. The study of these features in later Quaternary deposits has led to major developments in the identification and interpretation of landslide deposits in the geologic record. Morphologic features, such as hummocks, ridges, large surficial blocks, or faults have been used to determine landslide kinematics (e.g., van Wyk de Vries et al., 2001; Kelfoun and Druitt, 2005; Dufresne and Davies, 2009, Shugar and Clague, 2011; Paguican et al., 2014). Preservation of source stratigraphy has been described at numerous deposits of large ($>10^6$ m^3) landslides (e.g., Heim, 1932; Yarnold and Lombard, 1989; Vallance et al., 1995; Abdrakhmatov and Strom, 2006; Geertsema et al., 2006; Hewitt et al., 2008; Dufresne et al., 2009; Weidinger et al., 2014; Roverato et al., 2015) and is a characteristic feature of these mass movement types. Preserved source stratigraphy implies consistent laminar flow of the debris over long runout distances despite, in some cases, significant topographic interference. Smearing out and thinning of units or radial distribution of the initial sequence due to lateral spreading is common (e.g. Hewitt et al., 2008; Strom, 2006; Shugar and Clague, 2011; Dufresne et al., 2016a). A three-part depositional facies model consisting of (1) a coarse, largely unfragmented upper unit or carapace, (2) a finer-grained body facies of diverse sedimentology, and (3) a basal facies or basal mixed zone in contact with and often mixed or mingled with runout path sediments is commonly described (Heim, 1932; Yarnold and Lombard, 1989; Dunning, 2004; Abdrakhmatov and Strom, 2006; Shugar and Clague, 2011; Weidinger et al., 2014; Dufresne et al., 2016b). Further sub-facies within the heterogeneous body facies can include (a) a transitional (blocky) facies with block-in-matrix fabric at the contact between carapace and body, (b) jigsaw-fractured clasts and facies, (c) a fragmented facies where fragments of all sizes are in contact with each other, and (d) very fine-grained shear zones (Dufresne et al., 2016b; Dufresne and Dunning, 2017). Application of this facies model aids in correctly identifying origin and original extent of eroded and buried deposits of large landslides.

In this study, we investigate the 17 October 2015 landslide in Taan Fiord, Alaska (**Fig. 1)** (Haeussler et al., 2017; Higman et al., submitted) which offers a unique opportunity to study landslide behavior in different environments: supraglacial, on land, and subaqueous. It is indeed rare to find a single slope failure event covering such diverse runout path conditions. Our findings help determine which signatures of large landslides may remain in the geologic record over longer time-scales, and will help reduce the challenges associated with identification of past and future geological hazards in high latitude settings.

2. Geologic Setting and the 2015 Landslide

2.1 Geologic setting

Taan Fiord is located in the St. Elias Mountains of coastal southeastern Alaska (**Fig. 1**). The St. Elias Mountains are the world's highest coastal mountain range and are the result of ongoing oblique collision of the Yakutat terrane with North America (Plafker et al., 1987; Chapman et al., 2008; Worthington et al., 2012). Within this region, the Chugach-St. Elias orogen experiences rapid exhumation (Enkelmann et al., 2015), with up to 37 mm/a of convergence (Elliott et al., 2013). A series of major thrust faults associated with the Yakataga fold-thrust belt accommodate extremely high strain gradients in Icy Bay and at the foot of Mount St. Elias (Elliott et al., 2013; Chapman et al., 2015). Northwest of Taan Fiord, transform or oblique slip faulting along the Bagley Ice Field (Bruhn et al., 2012) links to the Fairweather transform fault to the east (Plafker, 1994), whereas to the west the Yakataga fold-thrust belt soles into the Yakutat megathrust (Pavlis et al., 2012). Offshore, the Yakataga fold-thrust belt becomes the Pamplona Zone and at depth the Yakutat megathrust links to the Aleutian megathrust (Worthington et al., 2010; Gulick et al., 2013).

The failure slope of the 2015 Taan landslide lies along the EW-oriented Chaix Hills Thrust fault, which is bounded by several known stratigraphic units, notably the Kulthieth Formation (relatively weak metasediments) to the north and the Yakataga Formation (weakly lithified glacial and

glaciomarine layers) in the southern block (e.g., Eyles et al., 1991; Plafker et al., 1994; Meigs et al., 2006; van Avendonk et al., 2013). The Taan landslide originated in interlayered sandstones, coal, mudstones, and conglomerates of the Kulthieth Formation of Miller (1957), dipping generally 25°N (**Fig. 2**). Meigs et al. (2006, their figure 3) report bedding striking NW with dips of 40 and 48° N near the failure scarp of the Taan landslide.

Taan Fiord, where the 2015 landslide occurred, is an arm of Icy Bay, which lies south of the Chugach-St. Elias Fault and in the Yakataga foreland thrust-system (Bruhn et al., 2004; Pavlis et al., 2012). High-relief, active faults with large-magnitude historical earthquakes (e.g., 1899 M8.2, plus seven earthquakes > M6 since 1958; Plafker and Thatcher, 2008, and references in Bruhn et al., 2004; Elliott et al., 2013), ongoing lower-magnitude seismicity, and accelerated deglaciation exposing steep and unstable slopes all increase the potential for catastrophic slope failures in the region.

2.2 The 17 October 2015 Taan landslide

On 17 October 2015, an estimated 60 x 10^6 m^3 rock mass (Haeussler et al., 2017; Higman et al., submitted) detached from as high as ~850 m above sea level at the terminus of Tyndall Glacier (**Figs. 1, 3**), a site of previous landsliding (Meigs et al., 2006). Approximately 90% of the mass entered directly into the fjord, creating a tsunami with runup of up to 192 m (Higman et al., submitted). Some debris re-emerged from the fjord on the opposite shore of Taan Fiord and on the eastern moraine, where it formed hummocky deposits typical of large landslides. Such re-emergence of debris onto land after travel through water has, to our knowledge, not been described before. A small portion of the landslide debris (~3%) slid onto Tyndall Glacier and a larger slide block remained within the source area (~7%).

Source stratigraphy (Kulthieth Formation; **Fig. 2**) is preserved in all subaerial debris. The catastrophic slope failure of 2015 was the result of the rapid retreat and thinning of Tyndall Glacier in the latter half of the 20th century, which by 1991 had retreated to its current position and exposed an oversteepened

slope mantled by loose ice-marginal deposits (Koppes and Hallet, 2006). Comparison of digital elevation models and optical satellite images shows that the catastrophic failure in 2015 was preceded by gradual slope deformation (Higman et al., submitted) since at least 1996 (Meigs et al., 2006).

3. Methods and Data

3.1 Field mapping and digital analysis

Field mapping of the subaerial landslide debris was conducted during several site visits between April and August 2016. Hummock ridge axis orientations were measured in the field and based on 25 October 2015 GeoEye imagery (pansharpened natural colour, resampled to ~0.5 m). The landslide sedimentology was studied in gullies and along fault planes within the slide block and at the distal hummocks, and structural measurements were taken of faulted bedding within the debris.

To document spatial variations in boulder size, we mapped individual clasts from the GeoEye image using the 'photo-sieving' method outlined in Shugar and Clague (2011). Individual boulders were digitized manually and the results evaluated using a neighborhood analysis. Each boulder polygon was first circumscribed using the Bounding Containers toolbox for ArcGIS, and length and width of the resulting rectangle were calculated. While they do not always perfectly circumscribe the blocks, rectangles provide a reasonable approximation for computing the dimensions of the boulders. For every non-overlapping 25x25 m square, the largest single block (a-axis, or length) was determined. The output is a raster map of maximum boulder size for the entire debris sheet.

Hummock perimeters were similarly digitized from a combination of high-resolution bathymetry, lidar, and orthophotos. Hummock polygons were then intersected with the DEMs to determine area, height, and other parameters using the Zonal Statistics to Table toolbox in ArcGIS.

The 0.5-m orthoimagery imposed a size limit for mapping features, thus a threshold of 1.5 m^2 as lower limit for the boulders and a 1-m minimum height for the hummocks was applied.

3.2 Bathymetry

Seafloor bathymetry was surveyed both from an Unmanned Surface Vessel (USV '*Jökull*') equipped with a Teledyne Odom MB2 multibeam echo sounder (MBES), and a larger vessel (USGS R/V '*Alaskan Gyre*') equipped with a Teledyne SeaBat T50P MBES, both collected simultaneously in August 2016. Sound velocity profiles were made with an AML MinosX and Xylem YSI CastAway. The USV Jökull and R/V '*Alaskan Gyre*' data were processed using HYPACK and Caris, respectively, following the cruise, and gridded to 1 m resolution. Processing steps included manual swath and subset editing and correcting for sound velocity, tides, pitch, yaw, and roll.

For the purpose of this paper, a simple morphological map resulting from the geophysical survey is sufficient. Detailed investigations of the submarine portion of the slide, including seismic data, are the focus of ongoing work (e.g., McCall et al., 2016).

4. Taan Landslide Sedimentology and Geomorphology

In the following section, we describe the Taan slide block and the landslide deposit in its three emplacement environments: debris on land, supra-glacial debris, and submarine deposition.

4.1 Source slide block and stratigraphy

Signs of ongoing slope deformation are pervasive throughout Taan Fiord and adjacent areas. It is therefore no surprise that the 2015 catastrophic failure was preceded by gradual slope motion / deep-seated gravitational slope deformation. Meigs et al. (2006) first identified an earlier, post-glacial-retreat rotational slide, observed around 1996 (**Fig. 3**), but no traces of a long-runout landslide deposit below waterline were documented at that time (Koppes and Hallet, 2006). Comparison of a series of DEMs between 2002 and 2016 revealed that a sequence of gradual slumping on the same slope prepared it for catastrophic failure (Higman et al., submitted) and is likely ongoing within the landslide mass (slide block) that remained at the bottom of the failure scarp. The top of this slide block displays intact surfaces of the original slope: trees are left standing (albeit tilted) and large (> 10 m across) blocks form an almost coherent surface of glacially polished rock (**Fig. 4A**).

A number of slide-related normal faults characterizes the slide block in the source area and suggests a translational sliding motion during deposition following the initial rotational failure. It is these normal faults that cause the debris to appear "striped" in aerial photographs (**Figs. 4B, C, 5A**): the crest of each slide block is covered with the coarser, ocher-brownish debris of the original, weathered surface, whereas the interior exposed along normal fault planes is material comminuted into much finer grain sizes (pebbles to clays), with fresh, bluish-grey outcrop surfaces. Overall, the debris arrested within the source area is rather coarse compared to longer-traveled debris (Dufresne et al., 2016): the fragmented facies, wherein grains of all sizes are typically in contact with each other and which is commonly composed of a wide spread of grain sizes (sub-µm to few cm), here is clast-supported with very little interstitial, fine-grained matrix present (**Fig. 4E, F**). Jigsaw-fractured clasts and boulders dominate the deposit surface (**Fig. 4D**), but are also pervasive within the interior. Coal layers, on the other hand, are often sheared and present the finest-grained units. Source stratigraphy and the pre-slide weathering profile, including a glacially polished rock surface, are preserved in the landslide deposit (**Fig. 4C**), but in places offset along shear planes.

4.2 Supra-glacial landslide debris

4.2.1 Morphology

The supraglacial landslide debris does not show much morphological variation (i.e., no hummocks); instead, an open network of large boulders litters a debris surface that mimics the underlying glacier surface topography (**Fig. 5**). The thickest deposits exposed along the calving face range up to about 10 m. These areas correspond to strips of deposit on the glacier that appear relatively thick, and are likely representative of the thickest portions of the supraglacial deposit as a whole, except where blocks slid into widening crevasses. Debris on the glacier was notably wetter (i.e., saturated throughout the debris thickness) than debris on the main landslide body, as observed during our June 2016 field campaign. It was also noticeably wetter than it was during preceding visits. It is possible that basal erosion and entrainment of glacier ice into the landslide debris and subsequent melting thereof explains the increased observed wetness.

4.2.2 Sedimentology

The variations in surface appearance (color and apparent grain sizes) result from differences in weathering and rock type; similar to the pattern in the debris arrested at the toe of the failure slope (see above). Rust-colored strips with abundant blocks > 1-m diameter originally belonged to the weathered surface of the slope, whereas dark bands without large blocks are exposures of the fragmented landslide interior (**Fig. 5**). Lighter-colored strips containing larger blocks are unweathered sandstone layers. All units are arranged in the original stratigraphic sequence, i.e., no mixing between the lithologic units occurred, indicating laminar flow of the debris (**Fig. 5B**).

4.3 Subaerial hummocks

4.3.1 Morphology

Some of the subaerial debris was deposited as a group of hummocks along the northeastern deposit margin (traveled across the fjord to deposit on moraines at the base of a vertical cliff; **Figs. 6A, 7, 8**), plus a single distal hummock on Hoof Hill Fan (**Figs. 6A, 9**). The hummock group (n=17) on the moraine consists of four large (~50 m diameter and up to 26 m height) and a number of smaller hummocks. Typically, the dominant long axes align parallel to inferred motion direction (Dufresne and Davies, 2009). At Taan, these hummocks indicate the beginning of lateral spreading at this location and show the angle of impact against the cliff: the long axes of the large hummocks are oriented obliquely to the cliff wall, whereas those of the small hummocks are oriented (sub-)perpendicular to the main travel direction. Hence, from an initial SE slope failure direction, the landslide debris forming this group of hummocks began spreading towards the ENE whilst traveling through the fjord waters. Stratigraphic layers of the smaller hummocks are faulted and tilted into near-vertical orientations (see below), indicating strong compaction of the debris upon collision with the cliff walls (see also Hewitt et al., 2008; Dufresne et al., 2016a). The tail-end of one hummock (**Fig. 8**) has a different ridge orientation. It diverts from the main travel direction as if the rear continued its forward motion after the front had stopped, but not sufficiently enough to detach and form another hummock.

The distal-most subaerial hummock (**Fig. 9**) was emplaced on Hoof Hill Fan, roughly 2.5 km and in an almost straight trajectory from the landslide source (**Fig. 6A**; note reconstructed long-axis in **Fig. 9C**); at 35 m height it is the largest subaerial hummock. It travelled roughly 1.5 kilometers completely submerged through the fjord (compare to landslide tsunami studies by, e.g., Fritz et al., 2009; Mohammed and Fritz, 2012), whose deepest point was 80-90 m below sea level, and re-emerged onto land to deposit to 15 m above sea level. Applying a very simple model often used in landslide studies for a first-order estimate of slide velocity (Jibson et al., 2006), in which only conversion of kinetic to potential energy is considered in $v=(2gh)^{0.5}$, results in a conservative estimate of its velocity of about 45 m/s (see also Higman et al., submitted).

4.3.2 Sedimentology

Source stratigraphy is preserved in all hummocks, and the layers are predominantly oriented horizontally in the large, and sub-vertically in the small hummocks in the group deposited on the moraine (**Fig. 8H**). The hummock depicted in **Fig. 8** shows the strongest evidence of successive deformation when the debris collided with topography. A white, partially disintegrated sandstone layer is faulted and buckled in two "arcs" (**Fig. 8C, D, H**). Where the two "arcs" meet is accordant with the aforementioned change in hummock long axis orientation (white lines in **Fig. 8A, H**).

Extensive gouge material with near-vertical beds, folds, and faults is exposed below the tide line at the group of hummocks (**Fig. 8E-G**). Although the basal contact to underlying, pre-slide sediments is not exposed, the proximity to the pre-slide topography proves this part to be the basal facies. The gouge is predominantly composed of sand- and mudstones. Some of the gouge is injected into the overlying fragmented landslide debris, forming diapirs (**Fig. 8G**). Shear bands are aligned with "trains" of jigsaw-fractured clasts at the body to basal facies contact (**Fig. 8F**). Gouge is also present as thin layers within the landslide debris near the base of the hummock on Hoof Hill Fan (**Fig. 9**). The basal gouge there is dominated by black coal. In fact, this entire distal hummock is mainly composed of mudstone and coal, again suggesting preservation of source stratigraphy and laminar flow of the

debris. The basal contact is exposed at the original elevation of the fan, and pebbles are found entrained into the landslide debris within ~ 0.5 m above this contact (**Fig. 9D**).

4.4 Subaqueous hummocks - morphology

Most of the 163 mapped submarine hummocks are emplaced downfjord from the subaerial population and many are (partially) buried by glacimarine sediments (McCall et al., 2016). A distinct size zonation was observed, with most of the very large features (> 20 m height) farther from the source area than the smaller ones (**Fig. 6A**). The hummock population is normally distributed by height (**Fig. 10B**), with most hummocks deposited between ~ 1.5 and ~ 2.5 km from source. Unlike the subaerial hummocks, those mapped along the fjord bottom did not exhibit a preferential ridgeline alignment with respect to the inferred flow direction(s) (**Fig. 6B**), with many being nearly perpendicular. However, burial by fjord sediments obscures the true geometry of the submarine hummocks (see also different trends in height versus area between the subaerial and the submarine population in **Fig. 10C**), yet several of the most southerly submarine hummocks are aligned in trains parallel to the downfjord motion direction.

4.5 Hummock and debris distribution

The size distribution of the hummocks (**Fig. 10A**) is positively skewed, with the vast majority of the submarine hummocks being smaller than ~ 10 m in height. However, it is important to keep in mind that most of the submarine hummocks are partially buried by up to ~20 m of glacimarine fines (McCall et al., 2016) that were either reworked and redeposited in the waning stages of the slide runout or at some time between the landslide/tsunami event and the marine surveys in summer 2016. The subaerial hummock sizes, on the other hand, are not skewed, with a fairly even distribution from < 5 to ~ 35 m in height (**Fig. 10A**). Overall, the hummock population shows several zones of deposition as far as the methods employed herein can imply (**Fig. 6**): the proximal area is almost void of hummocky deposition and is populated by the smallest visible mounds (or most affected by burial) at around one km into the fjord from the bottom of the source slope. These small mounds are followed radially outwards by larger structures with the tallest hummocks over 30 m in height. The single

hummock on Hoof Hill Fan sits aside from the main deposition as the only hummock that was deposited outside the tsunami backwash on this fan. Some patches of dark coal material are scattered on the lower elevation of Hoof Hill Fan and might be remnants of other re-emerged, but partially eroded, landslide debris. Thus, preservation of the total landslide extent was already compromised during emplacement.

Lateral spreading of the landslide not only deposited debris onto the glacier northward of the source, but also left rather subtle traces on the slopes to the immediate south (**Fig. 11**). A thin veneer of angular rubble covers the slope up to around 200 m asl and partially fills a series of gullies, destroying alder vegetation. These boulders may have been a spray of rock slide ejecta. This thin zone grades into a prominent ridge that demarcates the slide boundary as a trimline further downslope from 90 to about 50 m asl. Beyond this, the ridge disintegrates and appears washed, perhaps from a return tsunami wave.

4.6 Boulder distribution

The boulder distribution on the surface of Tyndall Glacier is characterized by a central region of large blocks (up to 30 m diameter), surrounded by a rim of smaller boulders (**Fig. 12**). The average boulder length (a-axis) of the supraglacial landslide debris is ~ 4.9 m. Landslide debris deposited on the lower part of the proximal slope, however, is skewed to the finer end of the grain size spectrum, with blocks more commonly < 10 m in diameter and none > 19 m. The average boulder length is the same as for the supraglacial debris, ~ 4.9 m. A conspicuous patch of large, grey boulders forms a rockfall fan high up on the south flank of the scarp (black circle in **Fig. 12**), with mean boulder lengths of 7.0 m and the largest being 25.4 m.

4.7 Shattered schist clasts

A peculiarity is the presence of shattered schist clasts at low elevations on the landslide deposit (**Fig. 13**). There are no schists in any of the rock units close to the landslide, and their source might be as far as Mt. St. Elias, according to the geologic map of Pavlis et al. (2012). The schist clasts were likely

transported to this location by the glacier. Enclosed (in an already shattered state) within ice blocks (**Fig. 13A, B**), they could have easily been picked up by the landslide or by the landslide-generated tsunami. Prior to that, they must have either rafted in the fjord waters or were broken off of the front of Tyndall Glacier upon impact by the landslide mass. The ice surrounding the schist clasts subsequently melted, leaving piles and rings of angular debris (**Fig. 13C, D**).

4.8 Rapid reworking of landslide deposits

4.8.1 Features absent from older landslide deposits

Larger blocks with "caps" (**Fig. 14A**) of finer clasts are widespread in the landslide debris arrested within the source area. Such caps have been observed by the authors on other very recent landslides (e.g., 2016 Lamplugh and 2002 Black Rapids Glaciers, Alaska, and several recent landslides in British Columbia, Canada), but are nowhere reported for ancient deposits. Likewise, miniature (<0.5 m high and across), fine-grained (predominantly < 5 cm) mounds (**Fig. 14B, C**) clustered amongst larger hummocks or in troughs between ridges are not known from older landslide deposits. The presence of these features, but absence in the geologic record, implies reworking and erosion over time.

4.8.2 Reworking of supraglacial debris

Much of the supraglacial debris is being rapidly transferred to and redeposited into the fjord by passive advection of fast flowing ice (moving over one km/a) (**Fig. 15**). Once transferred to the ice front, continuous rockfalls from the calving front (observed frequently during site investigations) are steadily transferring large amounts of supraglacial landslide material into the fjord, building a morainal shoal along the terminus that has already caused over half the glacier front to become grounded and cease calving. Differential bathymetry collected in June and August 2016 found that between 5-24 m of debris had been added to the fjord at the ice front in two months, and reduced fjord water depths at the calving front to less than 20 m. As the coarse blocks enter the shallowing fjord waters, fines are washed out with the tidal currents and redeposited more distally in the fjord.

The combination of rapid advection of the supraglacial debris to the glacier terminus building a shoal and impeding calving, and the additional load of the supraglacial debris on the ice surface, have both contributed to longitudinal stretching and surface lowering of the terminal zone of the glacier (**Fig. 16**). In the 12 months since the landslide occurred, the ice surface affected by the slide debris lowered significantly, by up to 70 m, and the terminus advanced approximately 350 m along its western margin (**Fig. 15**). By early 2017, almost all supraglacial debris was gone and the glacier terminus had advanced significantly, now covering the western half of the hummock group of **Fig. 7** (including the hummock shown in detail in **Fig. 8**).

4.8.3 Incision, erosion and burial

The slide block arrested in the source area showed 25 m deep gullies already formed within the few months between the earliest landslide imagery (25 October 2015) and the first site investigations (in April 2016) (**Fig. 16**). What appeared to be a 0.25 ha landslide lake with a 0.8 ha fan, that initially formed behind the slide block, has rapidly infilled to form a 9 ha fan ("infill" in **Fig. 16**), composed primarily of sands and silts, by May 2016.

5. Discussion

5.1 A landslide in three different environments

Each of the three emplacement environments of the 2015 Taan landslide (supraglacial, on land, and submarine) posed unique challenges to sedimentologic and stratigraphic investigations. Access to supraglacial debris was restricted due to the highly crevassed nature of the glacier surface, whereas submarine deposition can only be investigated remotely. The debris on land offered the most comprehensive survey of the characteristics of the Taan landslide deposit before most of it was destroyed by sudden re-advance of the glacier terminus.

5.2 Landslide sedimentology

The subaerial hummocks remained intact despite travelling roughly 1.0-1.5 km completely submerged through the fjord from a subaerial initiation zone and re-emergence onto land, climbing a total of some 100 m to the deposition sites. The stratigraphic sequence of the source rocks was preserved, i.e., no mixing between lithologic units occurred, and the sedimentology of the hummocks reflects the typical succession of large landslide deposits of a coarse upper carapace, a finer and heterogeneous interior body facies, and a heavily sheared and mixed basal zone (**Fig. 17A**; e.g., Dunning and Armitage, 2011). Not even the tsunami dynamics left visible traces in or on the hummocks, even though experimental and numerical studies by Fritz et al. (2009) and Mohammed and Fritz (2012) demonstrated that the water displaced by a landslide immediately roles back onto the moving granular mass, which should have caused some turbulence in the upper landslide mass. The tsunami's only legacy with respect to the Taan landslide was rather in eroding features in its direct path and suspending fines that later, together with glacier outwash, buried the submarine landslide deposit.

The slide's deposition around a fjord and onto a calving glacier immediately exposed the landslide interior and its base at the glacier contact, or at low tide for the onland hummocks, thus revealing the entire top-to-bottom sequence with the aforementioned three-part facies division (**Fig. 17B, C**). The well-exposed sedimentology of the subaerial mounds at Taan is unlikely to be misinterpretated as glacial moraines. Moraines consist of chaotic assemblages of material mixed from different sources and transported by glacial ice (Hambrey, 1994). Landslide deposits, on the other hand, are the product of brittle fracture, and rock types tend not to mix but remain in their original stratigraphic order. Even structures of the original rock mass are preserved despite crushing to powder-sized fragments, and the fine fraction is characterized by angular fragments, whereas moraines tend to have their fines washed out or they are composed of rounded grains (Reznichenko et al., 2011).

5.3 Debris distribution and landslide dynamics

Where runout paths are more or less unobstructed, hummock sizes and number density often decrease with distance from source in large landslides (Ui, 1983; Siebert, 1984; Glicken, 1996; Dufresne et al., 2009; Yoshida et al., 2012; Paguican et al., 2014). At Taan, a first glance at the hummock distribution

from the bathymetric data suggests the reverse (e.g., **Fig. 6**), where those with the largest planform area are farthest from the source. These are most likely compound hummocks (e.g., Clavero et al. 2002), i.e., individual hummocks that are amalgamated to each other (some forming long ridges, others more complex shapes). Examining the data by hummock height (**Fig. 10B**), on the other hand, indicates that the tallest hummocks traveled only about half as far as the most distal ones. Furthermore, preliminary seismic investigations in the fjord indicate that many submarine hummocks are surrounded and covered by a laminated facies up to 20 m thick in places, and that some of the smaller proximal hummocks are completely buried in fines, and hence not visible in the bathymetry (McCall et al., 2016). Further interpretation of the seismic data in work to come will improve the hummock distribution map.

Large landslides also create typical morphologies of hummocky landscapes, radial or longitudinal alignments of hummocks and ridges, intricate response to topography (such as overtopping obstacles even of a few hundreds of meters in height or runup), and single hummocks (toma) as well as mobilized runout-path sediments that extend beyond the main landslide deposition (Sassa and Wang, 2005; Prager et al., 2006; Dufresne, 2012). Hummock ridge axis orientations at Taan document both radial and linear spreading of the landslide debris, particularly in the subaerial hummocks where post-depositional burial did not alter their true geometries as must be assumed for most of the submarine debris. Radial spreading thus commenced immediately after failure, i.e., once the debris struck the runout path.

Geomorphometry and structures of the subaerial hummocks furthermore document differential motion of the debris where it collided with steep topography. The small hummocks of the subaerial group are situated between the large hummocks and the cliff they ran up against. Their long axes are oriented transverse to motion direction and stratigraphic layers are tilted to the near-vertical. Both features imply strong compressional components; which is evident in this context, but may aid in reconstructing motion mechanics in ancient deposits that lack the observational context. The large

hummocks record this collisional regime in bulging and faulting of rock units (compare to **Fig. 8D, H**) and rotation of the tail end of one particular hummock (**Fig. 8A**).

5.4 Supraglacial deposition

Supraglacial landslides often lack a distinct carapace, are somewhat thinner (few meters rather than tens of meters), and much more mobile than their counterparts on land, often resulting in greater runout distances (Evans and Clague, 1998; Jibson et al., 2006; Shugar and Clague, 2011). Hummocks are usually absent and longitudinal ridges are much more common, typically stretching into very long (km-scale), thin flowbands (Jibson et al., 2006; Dufresne and Davies, 2009; Shugar and Clague, 2011, Shugar et al., 2013). The supraglacial debris at Taan does not display any flowbands, and sorting of the supraglacial boulders is poor. The largest boulders are concentrated in the center of the supraglacial debris, which may be interpreted as a flow structure and is contrary to block distributions on other supraglacial landslides, where the largest blocks tend to be concentrated along the debris margin (Shugar and Clague, 2011, and references therein). Absence of flowbands and the reverse block distributions at Taan are most likely the result of very short travel (only ~ 400 m) across Tyndall Glacier, its very rough ice surface with large crevasses, and the sloping surface of the glacier. Source stratigraphy, however, was preserved in this depositional area despite the rough runout path conditions (**Fig. 5B**).

5.5 Applying process knowledge to identify ancient deposits

From the few subaerial hummocks alone, local travel directions were reliably reconstructed through morphometry (ridge long-axes orientations) and structural data (offset and faulted stratigraphic units). Kulthieth Formation rock units narrow down the source of the debris. All subaerial landslide hummocks preserved intact lithologic stratigraphy, indicating they are indeed mass movement rather than erosional or constructional features, which clearly differentiates them from any moraines (Reznichenko et al., 2012). If this had been an unobserved ancient deposit of unknown origin, these pieces of evidence would have already been sufficient to pinpoint the type of event (landslide) and its

source (motion direction indicators combined with intact stratigraphic sequence), and when compared to hummock sizes of recent landslides, like this study, would also give an approximation of the size of the event.

5.6 Rapid denudation and the geologic record

The morphology of the upper part of the Taan landslide at the source scarp suggests large scale rotational movement, with a translational component. The preserved, but fractured, surface of the main slide block is characterized by glacially sculpted bedrock, similar to the adjacent, slightly higher slope outside of the landslide. Without knowledge of the 2015 landslide, this glacial polish would be recorded in the sedimentary record at an elevation inconsistent with its conditions of formation.

In addition, the three emplacement environments support very different degrees of preservation in the geologic record. Depending on climate, landslide volume, material type, and catchment dynamics, large landslides can be well-preserved; some for millions of years (e.g., Breccia deposits in dry climates; Yarnold and Lombard, 1998), some for millennia (e.g., spreads in sensitive clays; Geertsema et al., 2017), and some from centuries to decades (Bell et al., 2012). At Taan, much of the landslide deposit is obscured below fjord waters, and overall subject to rapid erosion, burial, and reworking in these dynamic, high-latitude glacial environments.

It is well-known for landslides covering parts of a glacier's ablation zone to cause (non-climatic-related) advances or even surges of the glacier (e.g. Gardner and Hewitt 1990; Vacco et al. 2010; Reznichenko et al. 2011; Shugar et al. 2012). The effect of landslides deposited onto a glacier terminus and, in turn, the rapid denudation of the landslide deposit by calving front erosion is little studied, partly because these events are rare. The part of the landslide debris that is deposited onto the terminal zone of a fast-flowing calving glacier will very rapidly be reworked as it is advected towards the calving front (e.g., McSaveney, 2002; Shugar and Clague, 2011; Uhlmann et al., 2012; Dunning et al., 2015) (**Fig. 15)**. Supraglacial meltwater streams remove the finer fraction of the landslide debris (e.g., Hewitt et al., 2008), jeopardizing future deposit interpretation (Reznichenko et al., 2012). As the

supraglacial debris of the Taan landslide continues to build a morainal shoal at the ice front, water depths are being sufficiently reduced so that Tyndall Glacier has begun re-advancing into the fjord, reactivating the tidewater advance cycle, and reworked almost all the landslide debris into proximal glacimarine deposits.

6. Conclusions

The work presented in this article shows how quick-response investigations of recent geological events and correct process understanding aid in understanding complex stratigraphic records of past dynamic environments. It also points out some previously undescribed features (small mounds between larger hummocks, boulders capped by finer debris) that escape preservation in the geologic record due to erosion soon after landslide deposition.

Detailed sedimentological and structural analysis of the subaerial landslide debris yielded information on its emplacement dynamics, such as spreading directions to reconstruct their paths of motion, which is important for ancient deposits of uncertain origin.

Rapid erosion of large landslide deposits in dynamic glacial environments emphasizes the need to study them as soon after emplacement as possible. Future legacies of these geologic hazards range from persisting landscape changes (large hummocks and (unstable) slide blocks, dammed river valleys, scarps that change drainage patterns, etc.) to subtle remains (redeposited supraglacial debris, buried or eroded hummocks, etc.) that take expert eyes to identify.

Acknowledgements

The work was funded by National Science Foundation grants EAR-1639643, EAR-1638898, EAR-1639010, EAR-1638931, EAR-1638979, EAR-1638434, the U.S. Geological Survey, Virginia Tech,

Canada National Science and Engineering Research Council RGPIN 402225-11 to MK, the Oceans Alaska Science and Learning Center. DB acknowledges the support of the UW Mary Cline and Mary Gates awards. This is UTIG Contribution #3136. The text benefitted from USGS internal review by Evan Thoms. We thank the journal editor in chief Japser Knight, guest editor Peter Bobrowski, Stuart Dunning and an anonymous reviewer for helpful suggestions.

References

Abdrakhmatov, K., Strom, A.L., 2006. Dissected Rockslide and Rock Avalanche Deposits; Tien Shan, Kyrgyzstan. In: Evans, S.G., Scarascia-Mugnozza, G., Strom, A.L., Hermanns, R.L. (eds), Landslides from massive rock slope failure. Nato Science Series IV, Earth and Environmental Sciences 49, pp. 551-570.

Bell, R, Petschko, H., Rohrs, M., Dix, A., 2012 Assessment of landslide age, persistence, and human impact using airborne laser scanning digital terrain models. Geografiska Annaler: Series A, Physical Geography, 94, 135-156.

Bruhn, R.L., Pavlis, T.L., Plafker, G., Serpa, L., 2004. Deformation during terrane accretion in the Saint Elias orogen, Alaska: Geological Society of America Bulletin 116, 771–787.

Bruhn, R.L., Sauber, J., Cotton, M.M., Pavlis, T.L., Burgess, E., Ruppert, N., Forster, R.R., 2012. Plate margin deformation and active tectonics along the northern edge of the Yakutat Terrane in the Saint Elias Orogen, Alaska, and Yukon, Canada. Geosphere 8, 1384-1407.

Chapman, J.B., Pavlis, T.L., Bruhn, R.L., Worthington, L.L., Gulick, S.P.S., Berger, A.L., 2015. Structural relationships in the eastern syntaxis of the St. Elias orogen, Alaska. Geosphere 8, 105–126.

Chapman, J.B., Pavlis, T.L., Gulick, S.P., Berger, A.L., Lowe, L.L., Spotila, J.A., Bruhn, R.L., Vorkink, M., Koons, P., Barker, A., Picornell, C., Ridgway, K., Hallet, B., Jaeger, J., McCalpin, J., 2008. Neotectonics of the Yakutat Collision: Changes in deformation driven by mass redistribution. In: Freymueller, J.T., Haeussler, P.J., Wesson, R.L., Ekström, G. (eds). Active tectonics and

seismic potential of Alaska: American Geophysical Union Geophysical Monograph 179, pp. 65–81.

Clavero, J.E., Sparks, R.S.J., Huppert, H.E., Dade, W.B., 2002. Geological constraints on the emplacement mechanism of the Parinacota debris avalanche, northern Chile. Bulletin of Volcanology 64, 40-54.

Coe, J.A., Bessette-Kirton, E.K., Geertsema, M., 2017. Increasing rock-avalanche size and mobility in Glacier Bay National Park and Preserve, Alaska detected from 1984 to 2016 Landsat imagery. Landslides, doi:10.1007/s10346-017-0879-7.

Deline, P., Gruber, S., Delaloye, R., Fischer, L., Geertsema, M., Giardino, M., Hasler, A., Kirkbride, M., Krautblatter, M., Magnin, F., McColl, S., Ravanel, L., Schoeneich, P., 2015a. Chapter 15, Ice loss and slope stability in high-mountain regions. In: Haeberli, W., Whiteman, C., Shroder, J.F. Jr. (eds), Snow and Ice-related Hazards, Risks, and Disasters. Academic Press, Amsterdam, pp. 521-561.

Deline, P., Hewitt, K., Reznichenko, N. and Shugar, D., 2015b. Rock avalanches onto glaciers. In: Davies, T.R.H., Shroder, J.F. Jr. (eds), Landslide Hazards, Risks and Disasters. Elsevier, Amsterdam, pp. 263-319.

Dufresne, A., Dunning, S.A., 2017. Process-dependence of grain size distribution in rock avalanche deposits. Landslides. 14, 1555-1563.

Dufresne, A., Davies, T.R., McSaveney, M.J., 2009. Influence of runout-path material on emplacement of the Round Top rock avalanche, New Zealand. Earth Surface Processes and Landforms 35, 190-201.

Dufresne, A., Prager C., Bösmeier A., 2016a. Insights into rock avalanche emplacement processes from detailed morpho-lithological studies of the Tschirgant deposit (Tyrol, Austria). Earth Surface Processes and Landforms 41, 587-602.

Dufresne, A., Bösmeier, A., Prager, C., 2016b. Rock avalanche sedimentology – case study and review. Earth-Science Reviews 163, 234-259.

Dunning, S., 2004. Rock Avalanches in High Mountains. PhD thesis. University of Luton, UK, 337 pp.

Dunning, S.A., Armitage, P.J., 2011. The Grain-Size Distribution of Rock-Avalanche Deposits: Implications for Natural Dam Stability. Natural and Artificial Rockslide Dams, Lecture Notes in Earth Sciences 133, 479-498.

Dunning, S.A., Rosser, N.J., McColl, S.T., Reznichenko, N.V., 2013. Rapid sequestration of rock avalanche deposits within glaciers. Nature Communications 6, 7964, doi:10.1038/ncomms8964.

Ekström, G., Stark, C.P., 2013. Simple scaling of catastrophic landslide dynamics. Science 339, 1416-1419.

Elliott, J., Freymueller, J.T., Larsen, C.F., 2013. Active tectonics of the St. Elias orogen, Alaska, observed with GPS measurements, Journal of Geophysical Research Solid Earth 118, 5625–5642.

Enkelmann, E., Koons, P.O., Pavlis, T.L., Hallet, B., Barker, A., Elliott, J., Garver, J.I., Gulick, S.P.S., Headley, R.M. Pavlis, G.L., Ridgway, K.D., Ruppert, N., Avendonk, H.J.A., 2015. Cooperation among tectonic and surface processes in the St. Elias Range, Earth's highest coastal mountains. Geophysical Research Letters 42, 5838-5846, doi:10.1002/2015GL064727.

Evans, S.G., Clague, J.J., 1998. Rock avalanche from Mount Munday, Waddington Range, British Columbia, Canada. Landslide News 11, 23-25.

Eyles, C.H., Eyles, N., Lagoe, M.B., 1991. The Yakataga Formation, a late Miocene to Pleistocene record of temperate glacial marine sedimentation in the Gulf of Alaska. In: Anderson, J.B., and Ashley, G.M. (eds), Glacial-marine sedimentation; Paleoclimatic significance. Geological Society of America Special Paper 261, pp. 159–180.

Fritz, H.M, Mohammed, F., Yoo, J., 2009. Lituya Bay landslide impact generated mega-tsunami 50th anniversary. Pure and Applied Geophysics 166, 153-175.

Gardner, J.S., Hewitt, K., 1990. Surge of Bualtar Glacier, Karakoram Range, Pakistan: A Possible Landslide Trigger. Journal of Glaciology 36, 159-162.

Geertsema, M., Chiarle, M., 2013. Mass movement: effects of glacier thinning. In> Stoffel, M, Marston, R.A. (eds), Treatise on Geomorphology, Volume 7. Springer, Amsterdam, pp. 217-222.

Geertsema, M., Cruden. D.M., Clague, J.J., 2017. The landslide-modified glacimarine landscape of the Terrace-Kitimat area, BC. In: O. Slaymaker (ed). Landscapes and Landforms of Western Canada, World Geomorphological Landscapes. Springer International Publishing,. 349-361.

Geertsema, M., Hungr, O., Schwab, J.W., Evans S.G., 2006. A large rockslide-debris avalanche in cohesive soil at Pink Mountain, Northeastern British Columbia, Canada. Engineering Geology 83, 64-75.

Geertsema, M., Clague, J.J., Hasler, A. 2013. Influence of climate change on geohazards in Alaskan Parks. Alaska Park Science 12, 81-85.

Glicken, H., 1996. Rockslide-debris avalanche of May 18, 1980, Mount St. Helens, Washington. USGS Open-file Report 96-677, 90 pp.

Gruber, S., Haeberli, W., 2007. Permafrost in steep bedrock slopes and its temperature-related destabilization following climate-change. Journal of Geophysical Research Earth Surface 112(F2), doi:10.1029/2006JF000547.

Gulick, S.P.S., Reece, R.S., Christeson, G.L., van Avendonk, H.J.A., Worthington, L.L., Pavlis, T.L., 2013. Seismic images of the Transition Fault and the unstable Yakutat-Pacific-North American triple junction. Geology 41, 571-574.

Haeussler, P.J., Stark, C., Ekström, G., Gulick, S.S., Higman, B., Bloom, C., Bilderback, E., Dufresne, A., Geertsema, M., Guiltier, L., Jaffe, B., Koppes, M., Labay, K., Larsen, C., Loso, M., Lynett, P., McCall, N., Richmond, B., Reece, B., Shugar, D., Venditti, J., Walton, M., Weiss, R., Williams, H., 2017. The seismologically detected Taan Fiord landslide and tsunami of 17 October 2015: preliminary findings. Seismological Society of America Annual Meeting, Denver, Colorado, USA, 18-40 April 2017.

Hambrey, M.J., 1994. Glacial environments. UBC Press, Vancouver, 296 pp.

Heim, A., 1932. Bergsturz und Menschenleben (Landslides and human lives). Vierteljahrsschrift der Naturforschenden Gesellschaft in Zürich, 77, Beer & Co., Zürich, 218 pp.

Hewitt, K., 1999. Quaternary moraines versus catastrophic rock avalanches in the Karakoram Himalaya, northern Pakistan. Quaternary Research 51, 220–237.

Hewitt, K., Clague, J.J., Orwin, J.F., 2008. Legacies of catastrophic rock slope failures in mountain landscapes. Earth-Science Reviews 87, 1–38.

Higman, B., Shugar, D., Stark, C., Ekström, G., Koppes, M.N., Lynett, P., Dufresne, A., Haeussler, P..J, Geertsema, M., Gulick, S., Mattox, A., Venditti, J.G., Walton, M.A.L., McCall, N.,

McKittrick, E., MacInnes, B., Bilderback, E.L., Tang, H., Willis, M.J., Richmond, B., Reece, B., Larsen, C., Olson, B., Capra, J., Ayca, A., Bloom, C., Williams, H., Bonno, D., Weiss, R., Keen, A., Skanavis, V., Loso, M., 2017. An Alaskan landslide and tsunami induced by glacial retreat. Submitted.

Jibson, R.W., Harp, E.L., Schulz, W., Keefer, D.K., 2006. Large rock avalanches triggered by the M 7.9 Denali Fault, Alaska, earthquake of 3 November 2002. Engineering Geology 83, 144-160.

Kelfoun, K., Druitt, T.H., van Wyk de Vries, B., Guilband, M.N., 2008. Topographic reflection of the Socompa debris avalanche, Chile. Bulletin of Volcanology 70, 1169-1187.

Koppes, M., Hallet, B., 2006. Erosion rates during rapid deglaciation in Icy Bay, Alaska. Journal of Geophysical Research - Earth Surface 111, F02023, doi:10.1029/2005JF000349.

Kos, A., Amann, F., Strozzi, T., Delaloye, R., von Ruette, J., Springman, S., 2016. Contemporary glacier retreat triggers a rapid landslide response, Great Aletsch Glacier, Switzerland. Geophysical Research Letters 43, 12,466-12,474.

McCall, N., Walton, M., Gulick, S., Haeussler, P., Reece, R., Saustrup, S., 2016. Studying onshore-offshore fault linkages and landslides in Icy Bay and Taan Fjord to assess geohazards in Southeast Alaska. American Geophysical Union Annual Meeting Abstracts #EP41A-0895.

McColl, S.T., 2012. Paraglacial rock-slope stability, Geomorphology 153-154, 1-16.

McSaveney, M.J., 2002. Recent rockfalls and rock avalanches in Mount Cook National Park, New Zealand. In: Evans, S.G., DeGraff, J.V. (Eds.), Catastrophic Landslides: Effects, Occurrence, and Mechanisms. Geological Society of America, Reviews in Engineering Geology 15, pp. 35–70.

Meigs, A., Krugh, W.C., Davis, K., Bank, G., 2006. Ultra-rapid landscape response and sediment yield following glacier retreat, Icy Bay, southern Alaska. Geomorphology 78, 207-221.

Miller, D.J., 1957. Geology of the southeastern part of the Robinson Mountains, Yakataga district, Alaska: U.S. Geological Survey Oil and Gas Investigations Map, OM-187, scale 1:63,360.

Mohammed, F., Fritz, H.M., 2012. Physical modelling of tsunamis generated by three-dimensional deformable granular landslides. Journal of Geophysical Research 117, C11015, doi:10.1029/2011JC007850.

Paguican, E.M.R., van Wyk de Vries, B., Lagmay, A., 2014. Hummocks: how they form and how they evolve in rockslide-debris avalanches. Landslides 11, 67-80.

Pavlis, T.L., Chapman, J.B., Bruhn, R.L., Ridgway, K., Worthington, L.L., Gulick, S.P.S., Spotila, J., 2012. Structure of the actively deforming fold-thrust belt of the St. Elias orogen with implications for glacial exhumation and three-dimensional tectonic processes. Geosphere 8, 991–1019.

Plafker, G., 1987. Regional geology and petroleum potential of the northern Gulf of Alaska continental margin. In> Scholl, D.W., Grantz, A., Vedder, J.G. (eds), Geology and resource potential of the continental margin of western North America and adjacent ocean basins—Beaufort Sea to Baja California. Circum-Pacific Council for Energy and Mineral Resources, Earth Science Series 6, pp. 229-268.

Plafker, G., Thatcher, W., 2008. Geological and geophysical evaluation of the mechanisms of the great 1899 Yakutat Bay earthquakes. In: Freymueller, J.T., Haeussler, P.J., Wessen, R.L., Ekstrom, G. (eds). Geophysical Monograph 179, 215-236.

Plafker, G., Moore, J.C., Winkler, G.R., 1994. Geology of the southern Alaska margin. In: Plafker, G., Berg, H.C. (eds), The Geology of Alaska. Geological Society of America, pp. 389–449.

Prager, C., Krainer, K., Seidl, V., Chwatal, W., 2006. Spatial features of Holocene Sturzstrom-deposits inferred from subsurface investigations (Fernpass rockslide, Tyrol, Austria). GeoAlp 3 (147), 166.

Reznichenko, N.V., Davies, T.R.H., Alexander D.J., 2011. Effects of rock avalanches on glacier behaviour and moraine formation. Geomorphology 132, 327-338.

Reznichenko, N.V., Davies, T.R.H., Shulmeister, J., Larsen, S.H., 2012. A new technique for identifying rock avalanche-sourced sediment in moraines and some paleoclimatic implications. Geology 49, 319–322.

Roverato, M., Cronin, S., Procter, J., Capra, L., 2015. Textural features as indicators of debris avalanche transport and emplacement, Taranaki volcano. Geological Society of America Bulletin 127, 3-18.

Sassa, K., Wang, G.H., 2005. Mechanism of landslide-triggered debris flows: liquefaction phenomena due to the undrained loading of torrent deposits. In: Jakob, M., Hungr, O. (eds), Debris Flow Hazards and Related Phenomena. Springer Verlag, Berlin Heidelberg, pp. 81-104.

Shugar, D.H., Clague, J.J., 2011. The sedimentology and geomorphology of rock avalanches on glaciers. Sedimentology 58, 1762-1783.

Shugar, D.H., Clague, J.J., Giardino, M., 2013. A quantitative assessment of the sedimentology and geomorphology of rock avalanche deposits. In: Margottini, C., Catani, F., Trigila, A., Iadanza, C. (eds) Landslide Science and Practice, Vol 4: Global Environmental Change. Springer-Verlag, Berlin Heidelberg, pp. 321-326.

Shugar, D.H., Rabus, B.T., Clague, J.J., Capps, D.M., 2012. The response of Black Rapids Glacier, Alaska, to the Denali earthquake rock avalanches. Journal of Geophysical Research 117, F01006.

Siebert, L., 1984. Large volcanic debris avalanches: characteristics of source areas, deposits, and associated eruptions. Journal of Volcanology and Geothermal Research 22, 163-197.

Strom, A.L., 2006. Morphology and internal structure of rockslides and rock avalanches: grounds and constraints for their modelling. In: Evans, S.G., Scarascia-Mugnozza, G., Strom, A.L., Hermanns, R.L. (eds.), Landslides from Massive Rock Slope Failure. Nato Science Series IV, Earth and Environmental Sciences 49, pp. 305–328.

Uhlmann, M., Korup, O., Huggel, C., Fischer, L., Kargel, J.S., 2012. Supra-glacial deposition and flux of catastrophic rock-slope failure debris, south-central Alaska. Earth Surface Processes and Landforms 38, 675-682.

Ui, T., 1983. Volcanic debris avalanche deposits - identification and comparison with nonvolcanic debris stream deposits. Journal of Volcanology and Geothermal Research 18, 135-150.

Vacco, D.A., Alley, R.B., Pollard, D., 2010. Glacial advance and stagnation caused by rock avalanches. Earth and Planetary Sciences Letters 294, 123-130.

Vallance, J.W., Siebert, L., Rose, Jr. W.I., Girón, J.R., Banks, N.G., 1995. Edifice collapse and related hazards in Guatemala. Journal of Volcanology and Geothermal Research 66, 337-355.

van Wyk de Vries, B., Self, S., Francis, P.W., Keszthelyi, L., 2001. A gravitational spreading origin for the Socompa debris avalanche. Journal of Volcanology and Geothermal Research 105, 225-247.

Weidinger, J.T., Korup, O., Munack, H., Altenberger, U., Dunning, S.A, Tippelt, G., Lottermoser, W., 2014. Giant rockslide from the inside. Earth and Planetary Science Letters 389, 63-71.

Worthington, L.L., Gulick, S.P.S., Pavlis, T.L., 2010. Coupled stratigraphic and structural evolution of a glaciated orogenic wedge, offshore St. Elias orogen, Alaska. Tectonics 29, TC6013, doi:10.1029/2010TC002723.

Worthington, L.L., Van Avendonk, H. J.A., Gulick, S.P.S., Christeson, G.L., Pavlis, T.L., 2012, Crustal structure of the Yakutat terrane and the evolution of subduction and collision in southern Alaska. Journal of Geophysical Research 117, B01102, doi:10.1029/2011JB008493.

Yarnold, J.C., Lombard, J.P., 1989. A facies model for large rock avalanche deposits formed in dry climates. In: Colburn, I.P., Abbott P.L. and Minch J. (eds), Conglomerates in Basin Analysis> A Symposium Dedicated to A.O. Woodford, Pacific Section S.E.P.M., 62, pp. 9-31.

Yoshida, H., Sugai, T., Ohmori, H., 2012. Size-distance relationships for hummocks on volcanic rockslide-debris avalanche deposits in Japan. Geomorphology 136, 76-87.

Figure Captions

Figure 1. Setting of the 17 Oct 2015 Taan Fjord Landslide and Tsunami. The source rocks lie north of two faults that divide the Yakataga formation in the south, from the Kultieth formation in the north, providing the source rock for the landslide. The sliver of crust between the faults has been most recently mapped as Yakataga (Chapman et al., 2012).

Figure 2. (A) Sandstone clast with coal layer, and (B) mudstone clast in the landslide debris. (C) Overview of the uppermost landslide scarp of 2015 (section is roughly 300 m high and is a close-up of the area in the top left corner above the 1996 scarp (white dashed line) in **Fig. 3B**:). (D) Stratigraphy of the Kulthieth Formation (after Pavlis et al., (2012) and van Avendonk et al. (2013). The profile is from the hanging wall of the Chaix Hill fault and thus, within Taan Fiord the Kulthieth Fm. does not exist in its full thickness.

Figure 3. (A) The slope in 1996 (from Meigs et al. 2006) already displays signs of sliding. (B) The same view after the 2015 catastrophic failure (image taken in June 2016). (C) and (D) are DEMs

before (2000) and after (2016) the catastrophic failure. (C) Precursory slope deformations are discernable in the form of backscarps. (D) The large volume excavated from the source area, change in shore line and in the glacier terminal after loading by landslide debris are apparent.

Figure 4. (A) Glacial-polish on megablocks on top of slump. (B) Coloured bands on the landslide surface are a function of rock type, weathering coat, and grain size (compare to **Fig. 5**). (C) Preserved layers in slump debris. (D) In-situ fractured (= jigsaw-fractured) block. (E-F) Fragmented facies.

Figure 5. (A) Aerial view of the supraglacial landslide deposit and the slumped debris within the source area; red lines are slumps/normal faults, blue lines are active fluvial channels eroding deep gullies into the debris, and the white dashed-dotted line traces the approximate margin of Tyndall Glacier. (B) Conceptual sketch as a potential explanation for the striped appearance of the debris along a virtual profile x-x'.

Figure 6. Distribution map of hummocks based on lidar images and bathymetry data. The left panel shows hummock area and height, the right panel includes hummock ridges (white lines) and indicates landslide spreading direction based on hummock alignments, geomorphometry, and structural data. The two large hummocks downfjord are compound landforms. Solid lines are known landslide deposit boundaries, dashed lines infer this boundary.

Figure 7. Hummocks on land (east of the glacier, **Fig. 3B**) outlined in black; blue lines are ridge crests and the arrows show motion direction of the debris deduced from geomorphometric and structural data. Dashed line shows the deposit margin against the cliff bottom and dead ice mounds (dark shaded areas in contact to the cliff). See Figure 6 for location.

Figure 8. Deformation features within one of the subaerial hummocks (A-D) and the gouge material at its base (E-G). Blue dashed line (A) traces ridge lines (compare to Figure 6); white lines (A, H) connect the bend in ridge axis with structural features in the interior. White circle (C): person for scale.

Tilted layers (D), offset gouge (E), shear band (lower yellow line) parallel to aligned clast (upper yellow line; F), (G) diapir of gouge material. (H) is a simplified sketch of the hummock in (D) showing sub-horizontal layers in the large and sub-vertical layers in the small hummocks (black: coal layers; white: faulted sandstone unit); motion direction is roughly left to right (D, H). See Figure 6 for location.

Figure 9. Distal hummock on Hoof Hill fan. (A) Path of re-emergence after travel through the fjord water to the final deposition site on land. (B) View from Hoof Hill fan toward the landslide failure scarp with person for scale. (C) Reconstruction of hummock shape and long axis orientation; long axis length (dashed blue line) is 75 m. (D) The solid white line traces the original fan surface beneath the distal hummock and the dashed white line traces the elevation of entrained pebbles. See Figure 6 for location.

Figure 10. Statistics of hummock size and travel distance. (A) Histogram of hummock heights. (B) Scatterplot of hummock height and linear travel distance from common point in source area (see **Fig. 9**); as distances are straight-line, they should be treated as minima. (C) Scatterplot of area and height. All panels differentiate between subaerial and subaqueous hummocks. Note that many of the subaqueous hummocks are partly buried by fine sediment that has settled since the landslide occurred. As a result, those measurements should be treated as minima.

Figure 11.(A) Landslide traces beneath Daisy Glacier valley. (B) Field photo of scattered angular boulders taken from the area just below the two yellow arrows shows landslide debris draped over the slope. See Figures 6 and 12 for location.

Figure 12. Neighbourhood analysis of boulder size for the source area and supraglacial landslide deposit; the extent of the 2015 landslide deposit it marked by yellow dashed line. Coloured squares

represent 625 m^2 squares, and the largest boulder in each is mapped. The boulders inside the black circle belong to a separate, later rockfall event.

Figure 13. (A) and (B) schist fragments in ice block (approx. 1 m across in B); (C) and (D) shattered schist clasts within the hummock cluster (0.5 m long axe for scale).

Figure 14. (A) Megablocks covered with debris are quite common in this landslide deposit. Contrasting behaviours of different lithologies are also apparent in this photograph: coarse sandstone debris versus small mounds of finer-grained (< few cm) shale and coal in the background. Block with debris on top is roughly 0.5-1 m high. (B, C) Miniature mounds between ridges and larger hummocks.

Figure 15. Oblique photographs and time series of the changes at the terminus of Tyndall Glacier on (A) 21 March 2016 and (B) 6 August 2016. Note lowering of the ice surface in (B) and advection of the supraglacial landslide debris to the waterline. Red circles indicate the location of the largest hummock proximal to the ice front. (C) Outlines of the locations of supraglacial landslide debris from October 2015 until November 2016. The underlying image was taken in March 2016.

Figure 16. This photograph from May 2016 shows the rapid denudation of the glacier terminus, erosion of the landslide debris (gullies in the slide block and supraglacial debris advected into the fjord), and stretching of the glacier in response to landslide loading.

Figure 17. (A) Sketch of the typical three-part depositional facies model of large landslides; not to scale. The equivalent facies in the Taan landslide: (B) supraglacial debris (ice thickness above waterline is roughly 10 m; the boundary to overlying landslide debris is not clear since some areas of landslide debris look ice-cored with only a thin layer of fines draped over the cliff, hence the presence of a basal zone cannot be verified), and (C) hummock on land (compare to **Fig. 8**).

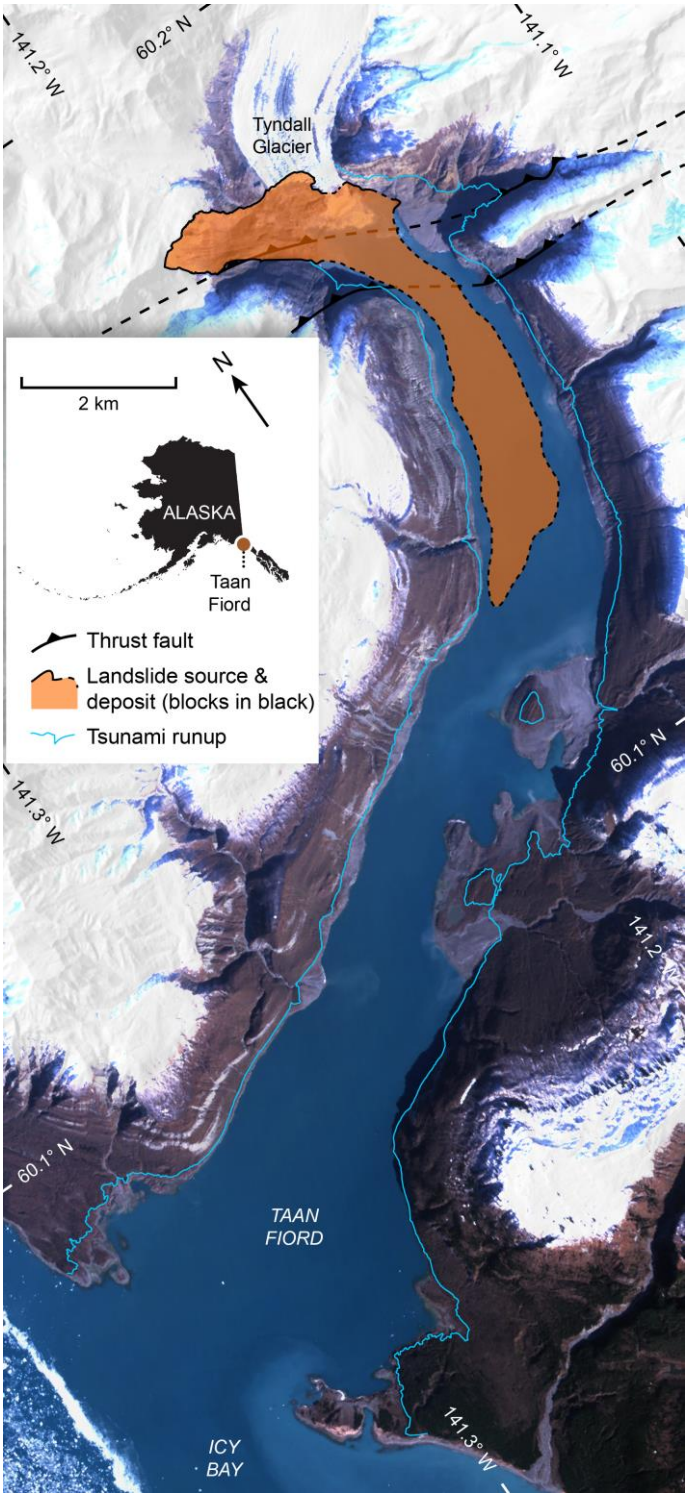

Figure 1

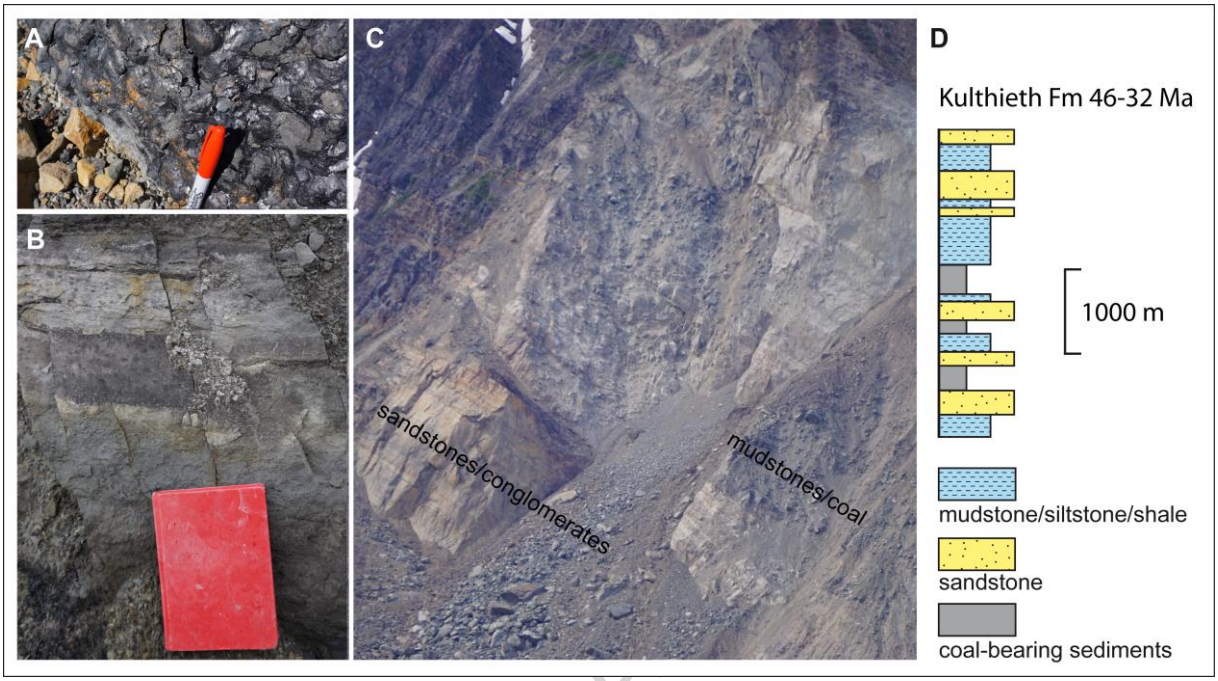

Figure 2

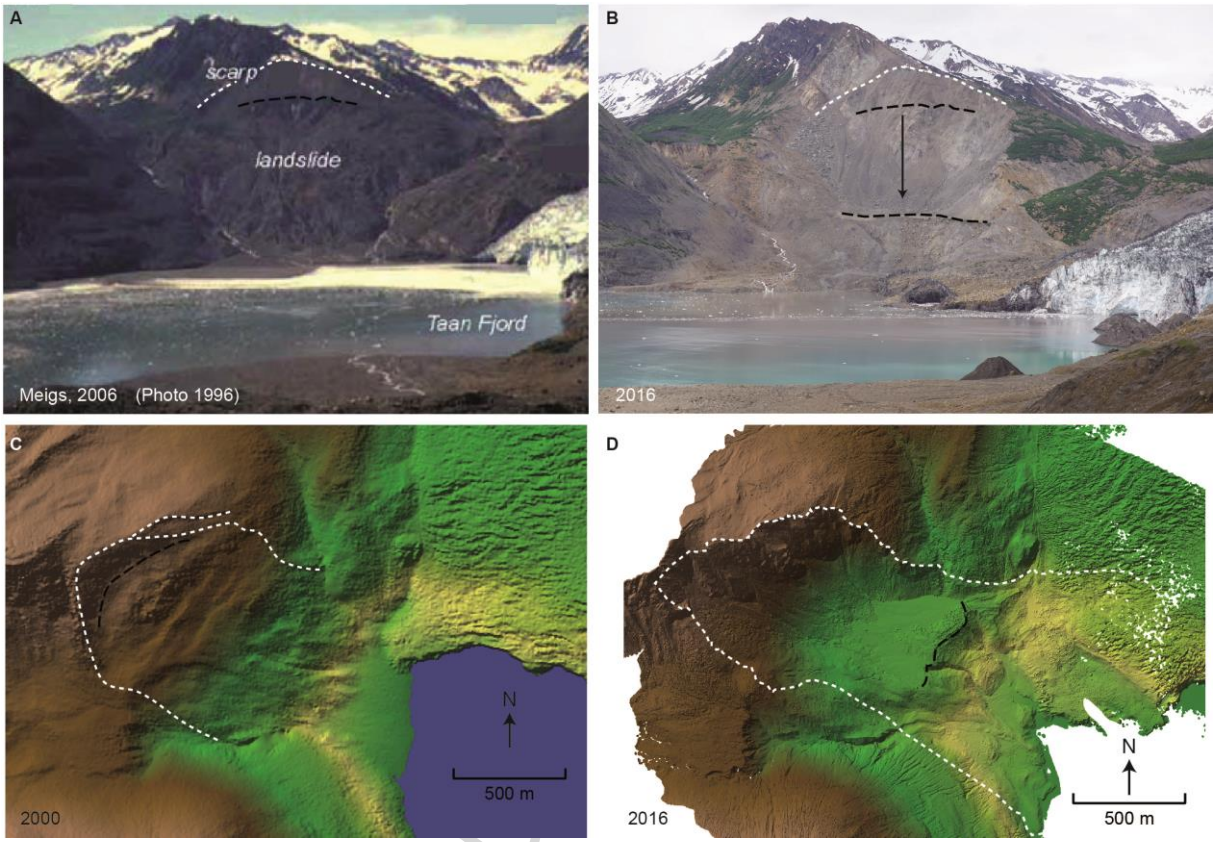

Figure 3

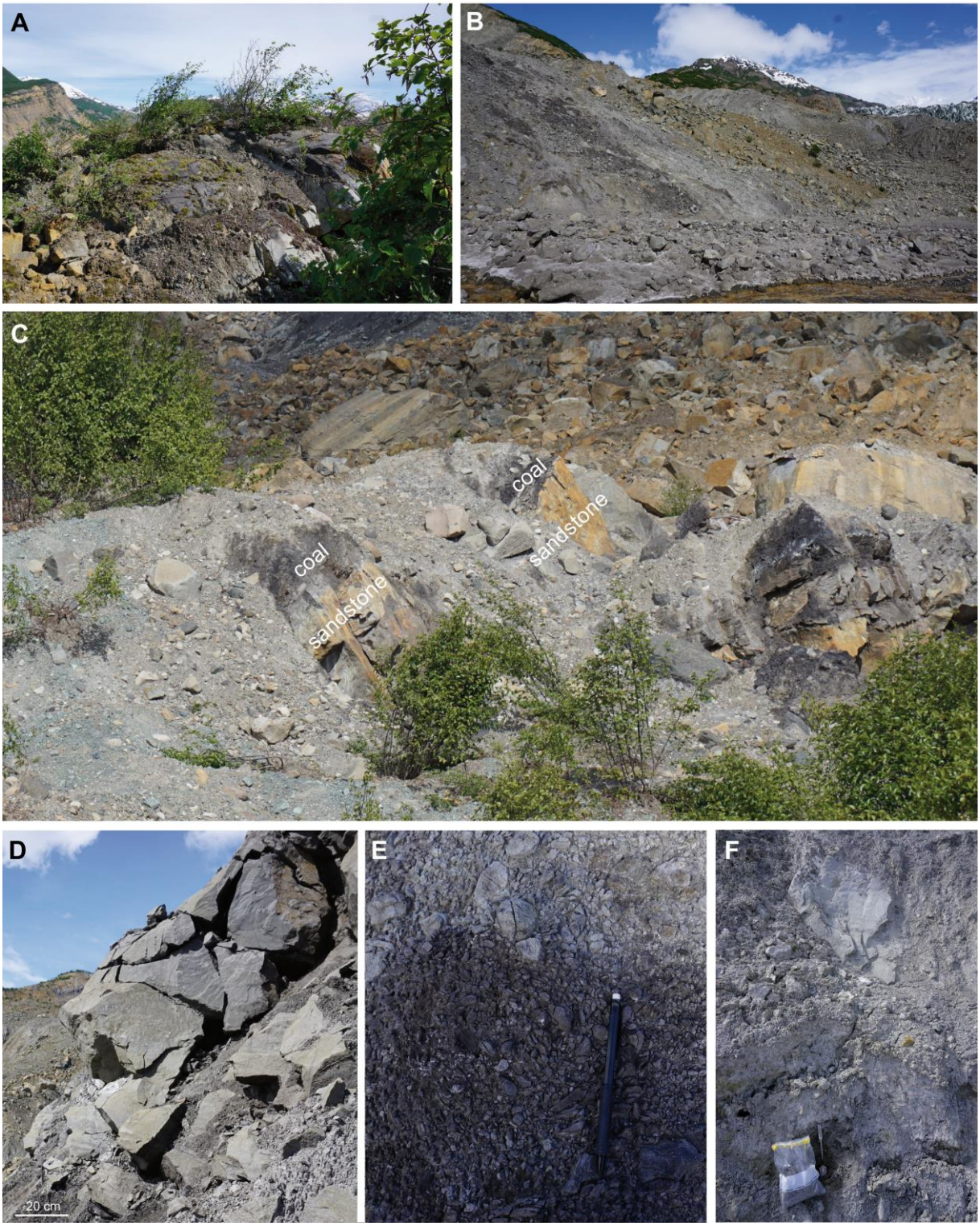

Figure 4

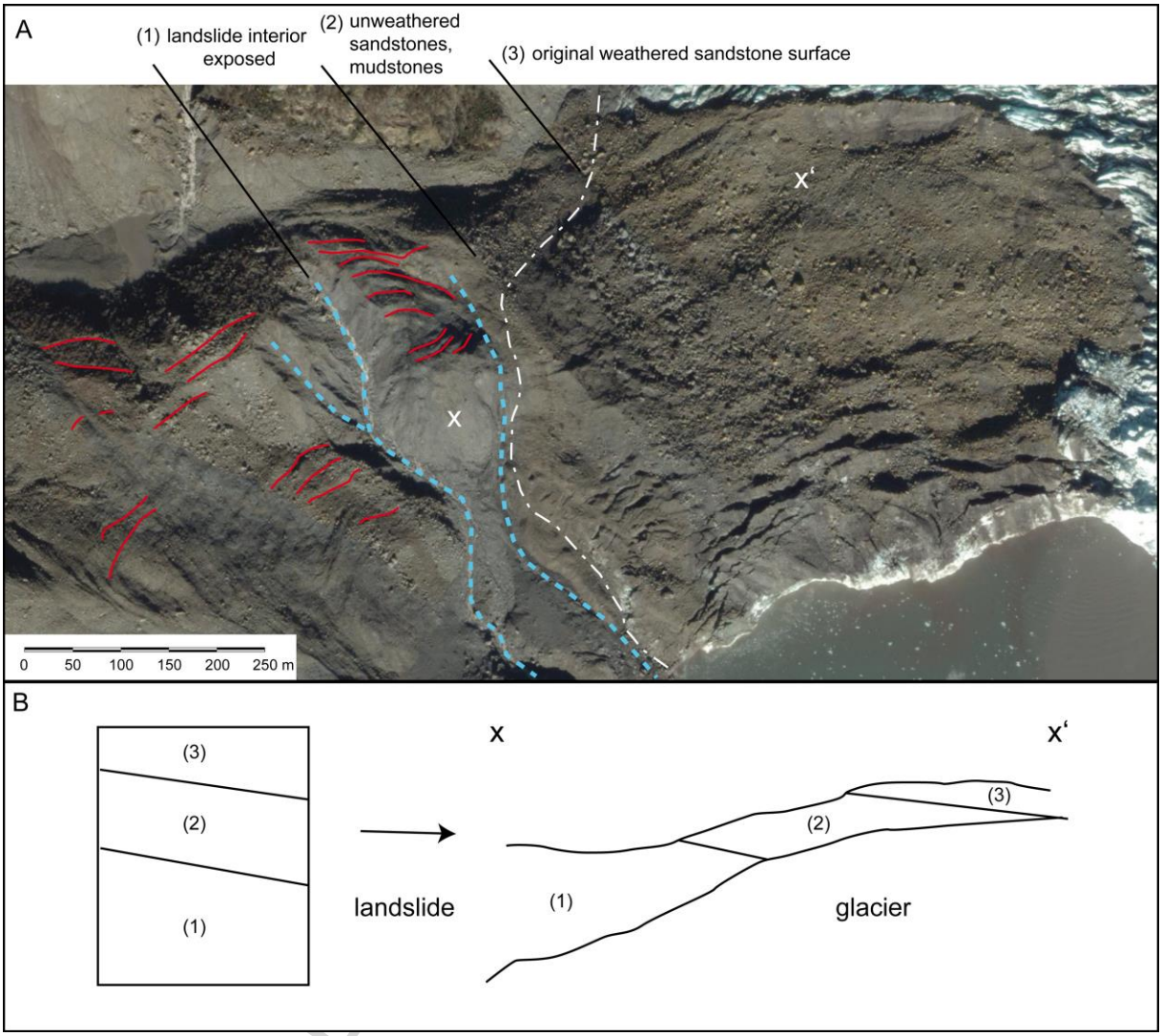

Figure 5

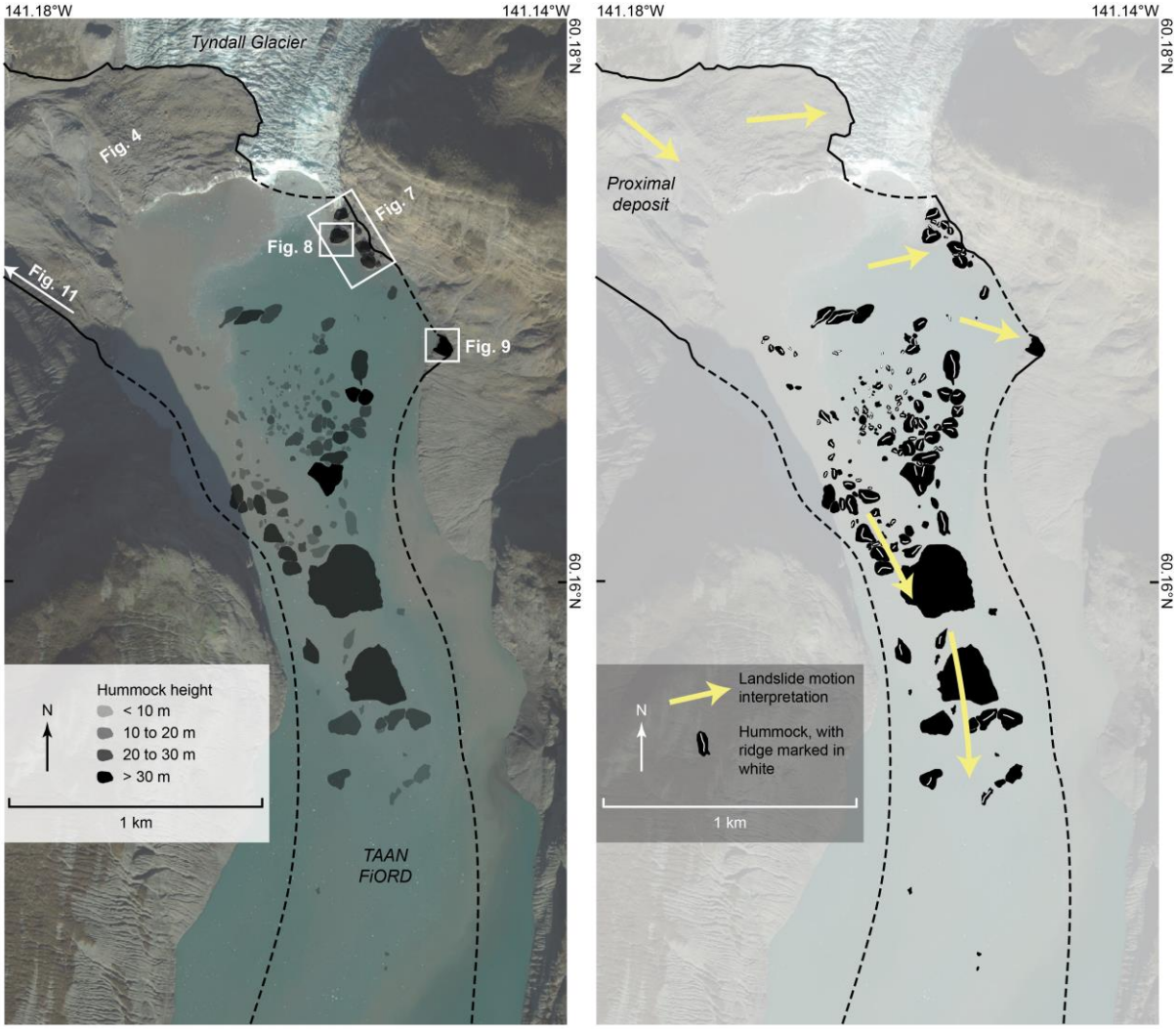

Figure 6

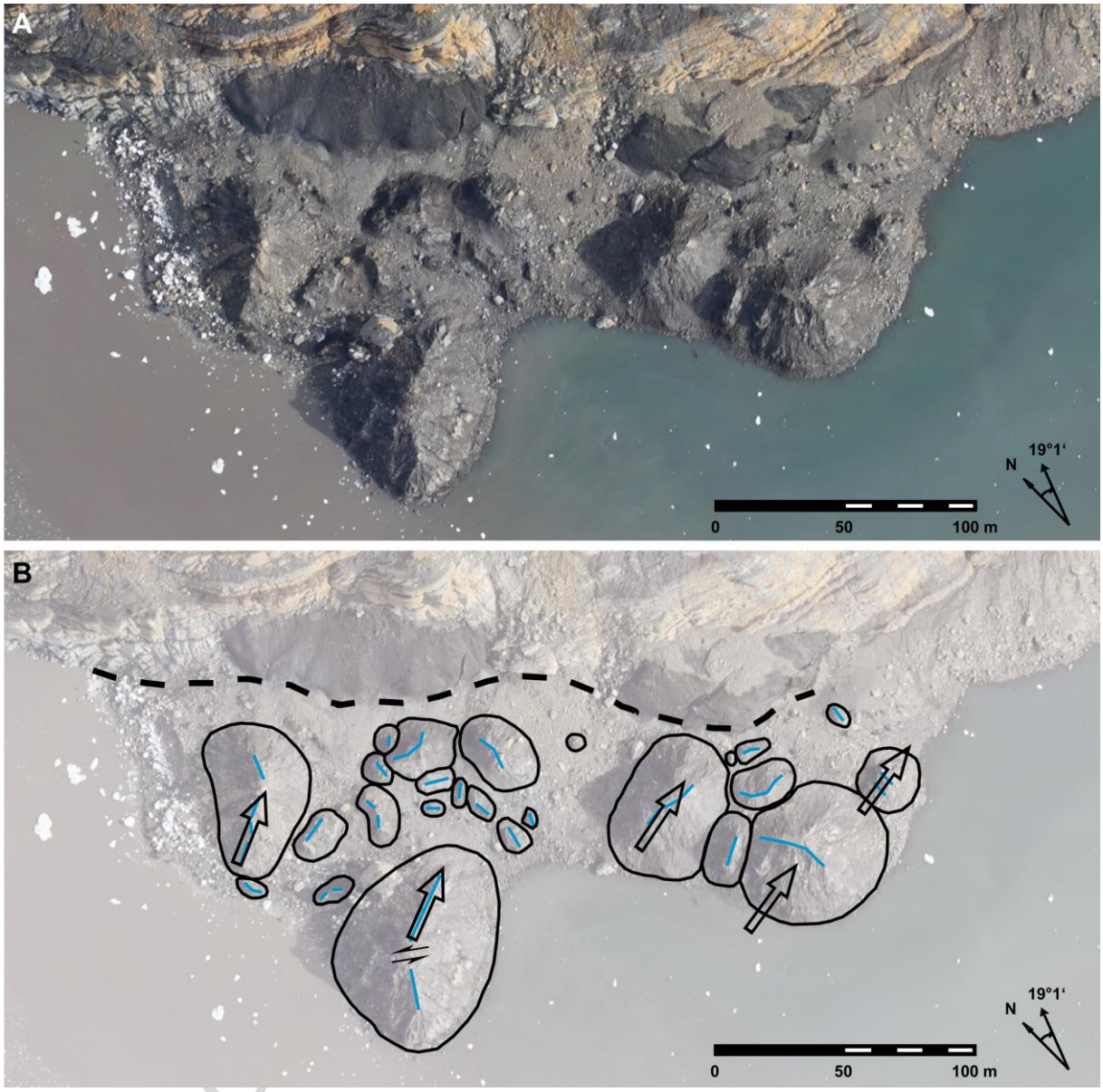

Figure 7

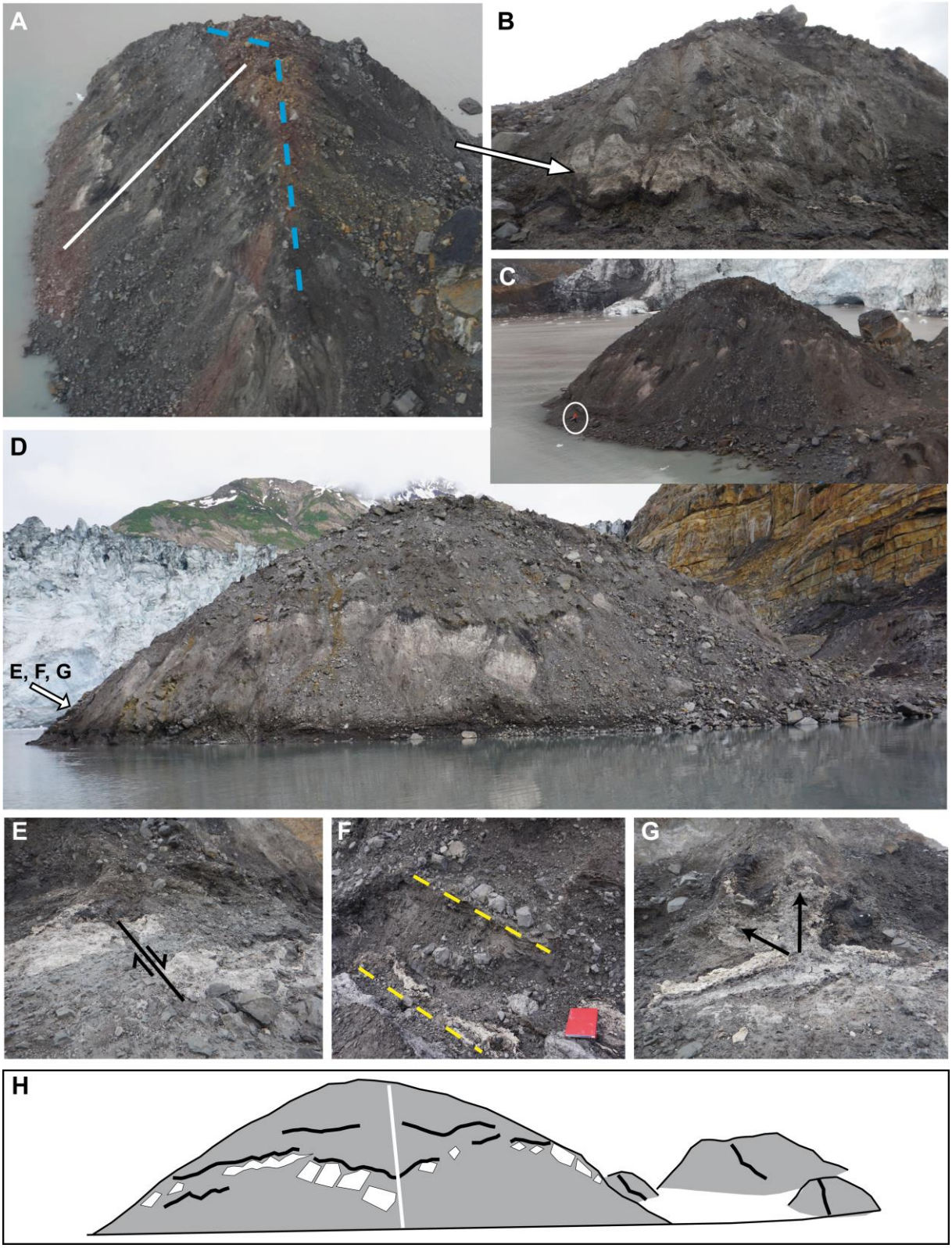

Figure 8

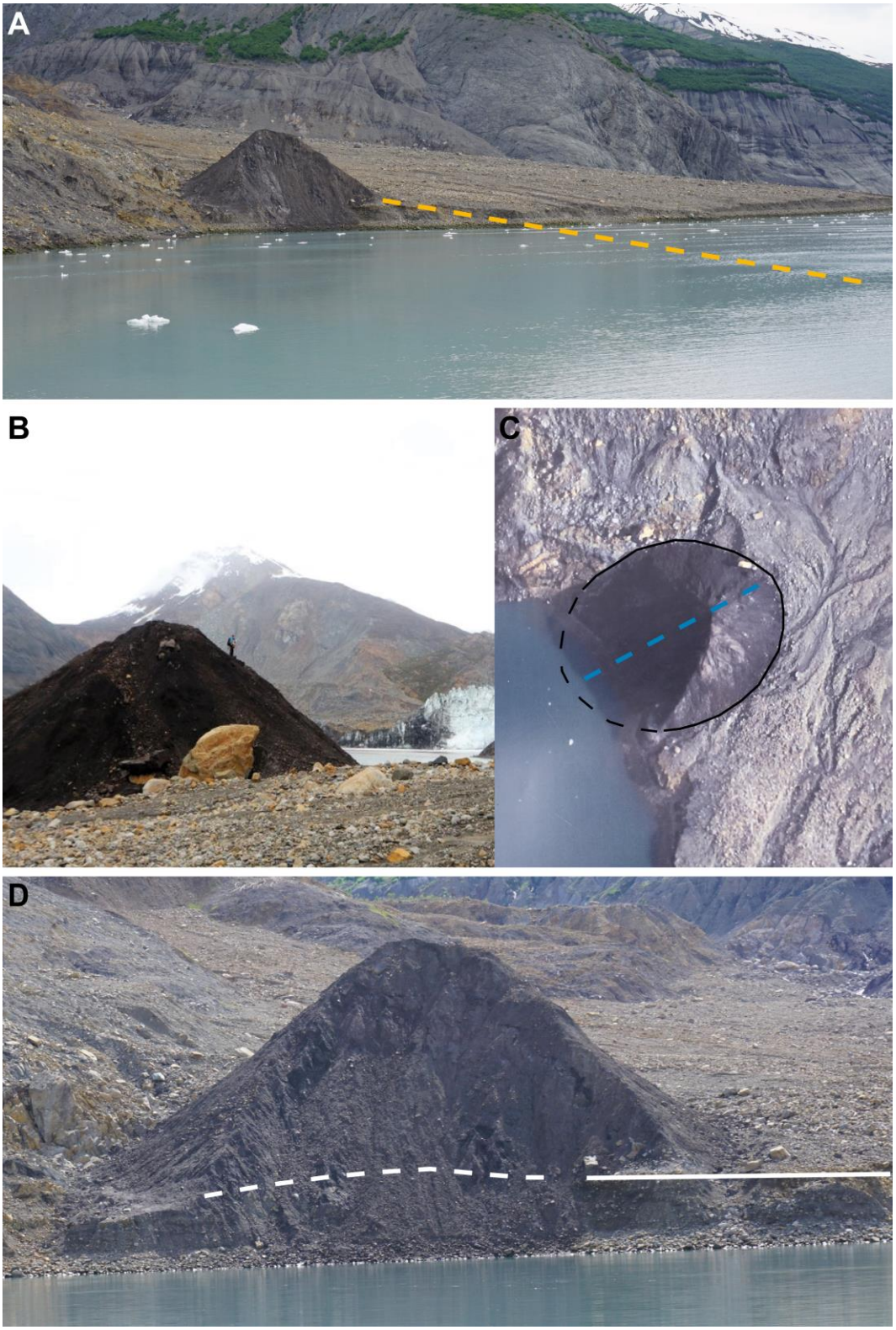

Figure 9

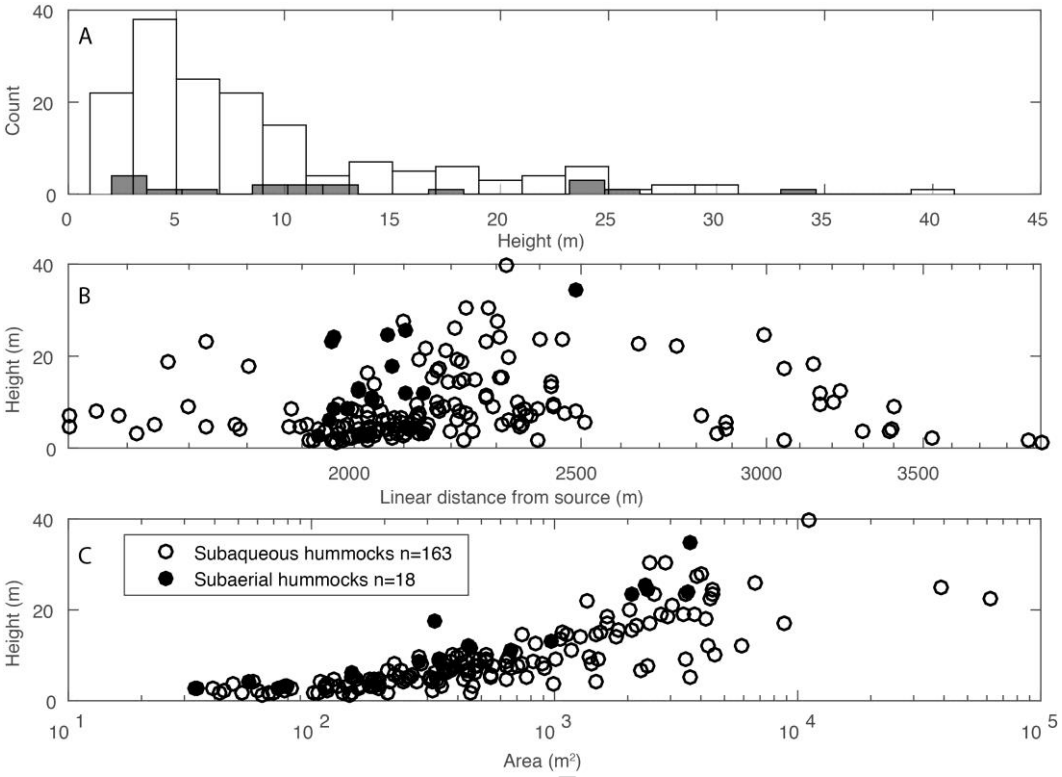

Figure 10

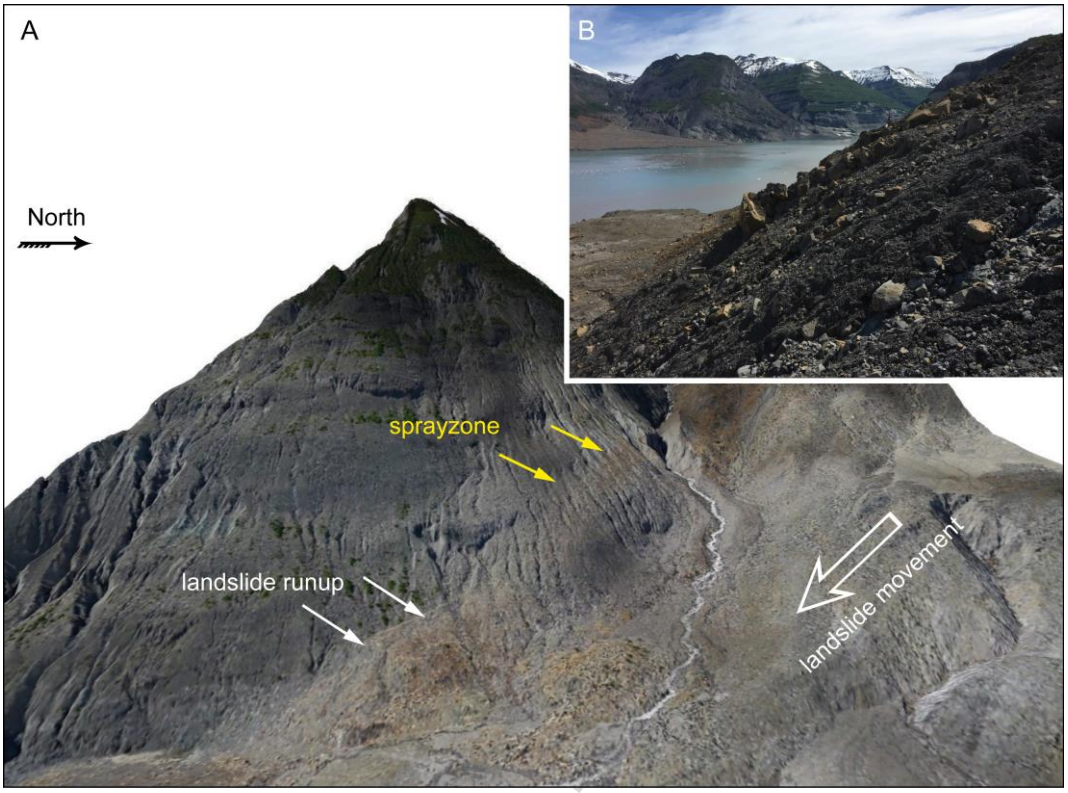

Figure 11

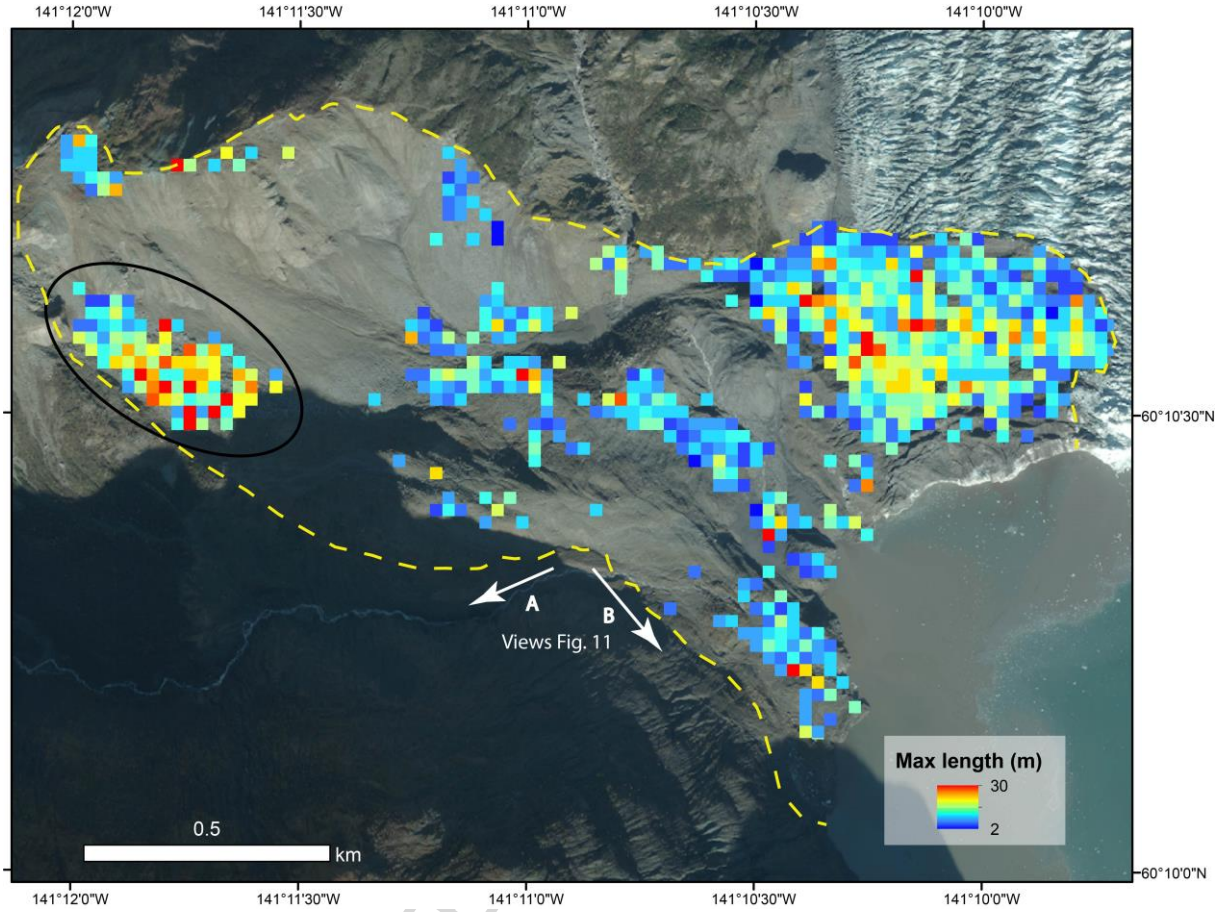

Figure 12

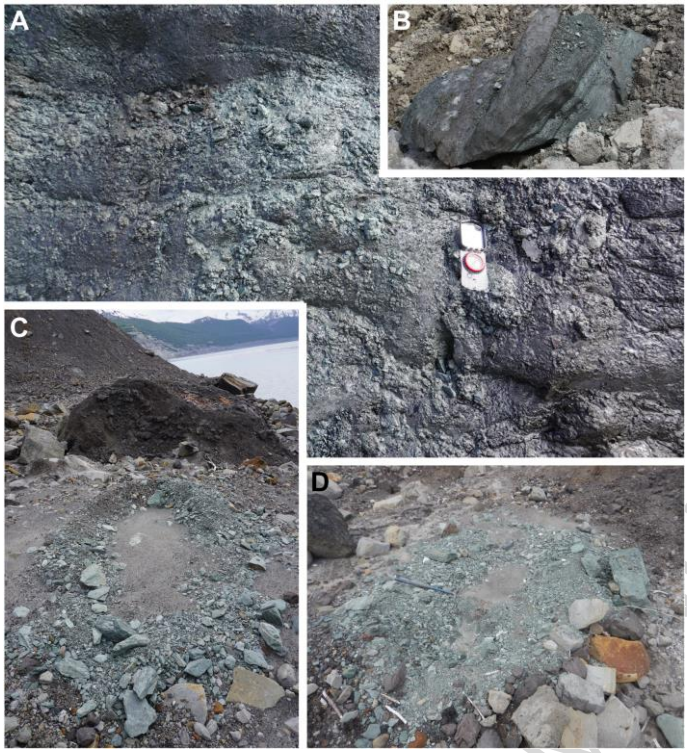

Figure 13

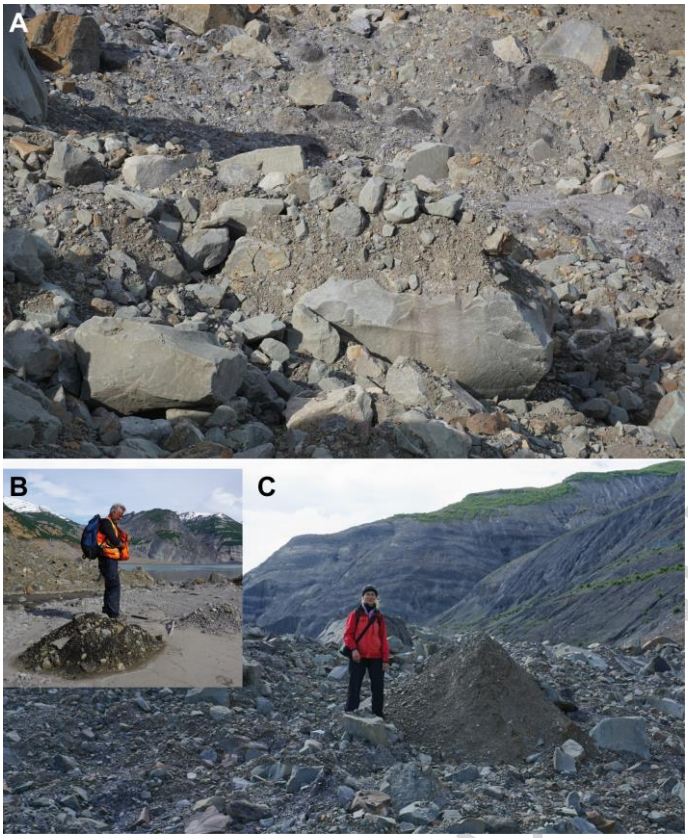

Figure 14

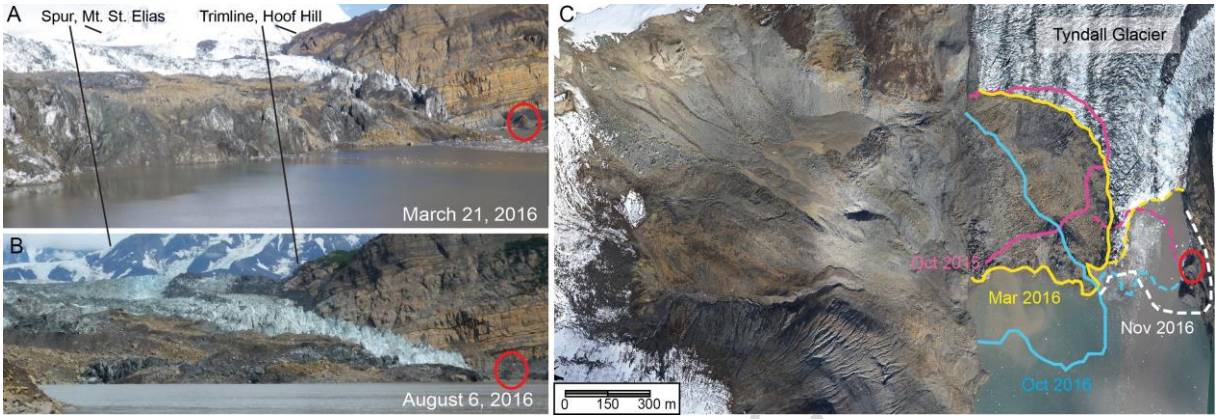

Figure 15

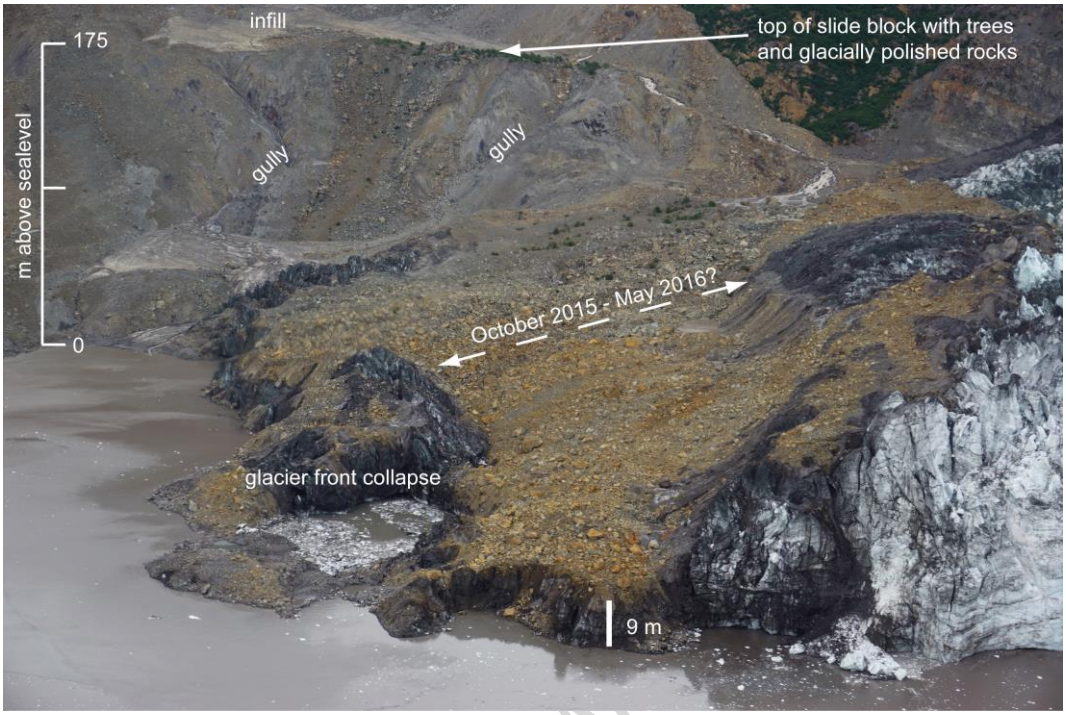

Figure 16

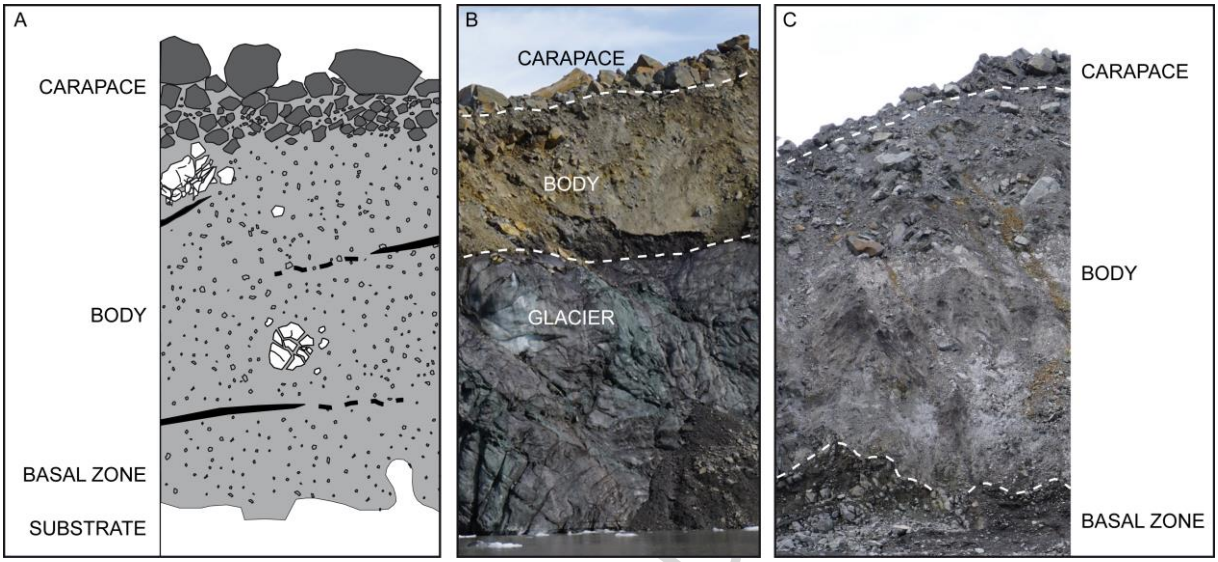

Figure 17